

Smoothing of sandpile surfaces after intermittent and continuous avalanches: three models in search of an experiment

Parthapratim Biswas*, Arnab Majumdar†
S.N.Bose National Centre For Basic Sciences
Salt Lake City, Block JD, Sector III
Calcutta-700 091, INDIA

Anita Mehta‡
S.N.Bose National Centre For Basic Sciences
Salt Lake City, Block JD, Sector III
Calcutta-700 091, INDIA
and
Institute of Theoretical Physics
University of California
Santa Barbara, CA 93106, USA

J. K. Bhattacharjee§
Department of Theoretical Physics
Indian Association for the Cultivation of Science
Jadavpur, Calcutta-700 032, INDIA

We present and analyse in this paper three models of coupled continuum equations all united by a common theme: the intuitive notion that sandpile surfaces are left smoother by the propagation of avalanches across them. Two of these concern smoothing at the ‘bare’ interface, appropriate to intermittent avalanche flow, while one of them models smoothing at the effective surface defined by a cloud of flowing grains across the ‘bare’ interface, which is appropriate to the regime where avalanches flow continuously across the sandpile.

PACS NOS.: 05.40+j, 05.70.Ln, 46.10.+z, 64.60.Ht

I. INTRODUCTION

The dynamics of sandpiles have intrigued researchers in physics over recent years [1,2] with a great deal of effort being devoted to the development of techniques involving for instance cellular automata [3,4], continuum equations [5–7] and Monte Carlo schemes [8] to investigate this very complex subject. However what have often been lost sight of in all this complexity are some of the extremely simple phenomena that are exhibited by granular media which still remain unexplained.

One such phenomenon is that of the smoothing of a sandpile surface after the propagation of an avalanche [9]. It is clear what happens physically: an avalanche provides a means of shaving off roughness from the surface of a sandpile by transferring grains from bumps to available voids [2,4], and thus leaves in its wake a smoother surface. However, surprisingly, researchers have not to our knowledge come up with models of sandpiles that have exhibited this behaviour.

In particular what has not attracted enough attention in the literature is the qualitative difference between the situations which obtain when sandpiles exhibit intermittent and continuous avalanches [10]. In this paper we examine both the latter situations, via distinct models of sandpile surfaces.

A particular experimental paradigm that we choose to put our discussions in context is that of sand in rotating cylinders [11,12]. In the case when sand is rotated slowly in a cylinder, intermittent avalanching is observed; thus sand accumulates in part of the cylinder to beyond its angle of repose [13] and is then released via an avalanche

*ppb@boson.bose.res.in

†Present address: Physics Department, Boston University, Boston, MA 02215 USA, E-mail: arnab@bu.edu

‡anita@boson.bose.res.in

§tpjkb@iacs.ernet.in

process across the slope. This happens intermittently, since the rotation speed is less than the characteristic time between avalanches. By contrast, when the rotation speed exceeds the time between avalanches, we see continuous avalanching on the sandpile surface. Though this phenomenon has been observed [13] and analysed physically [10] in terms of avalanche statistics, we are not aware of measurements which measure the characteristics of the resulting surface in terms of its smoothness or otherwise.

What we focus on here is precisely this aspect, and make predictions which we hope will be tested experimentally. In order to discuss this, we introduce first the notion that granular dynamics is well described by the competition between the dynamics of grains moving independently of each other and that of their collective motion within clusters [2]. A convenient way of representing this is via coupled continuum equations with a specific coupling between mobile grains ρ and clusters h on the surface of a sandpile [5]. In the regime of intermittent avalanching, we expect that the interface will be the one defined by the ‘bare’ surface, *i.e.* the one defined by the relatively immobile clusters across which grains flow intermittently. This then implies that the roughening characteristics of the h profile should be examined. The simplest of the three models we discuss in this paper (an exactly solvable model referred to hereafter as Case A) as well as the most complex one (referred to hereafter as Case C) treat this situation, where we obtain in both cases an asymptotic smoothing behaviour in h . When on the other hand, there is continuous avalanching, the flowing grains provide an effective film across the bare surface and it is therefore the species ρ which should be analysed for spatial and temporal roughening. In the model hereafter referred to as Case B we look at this situation, and obtain the surprising result of a gradual crossover between purely diffusive behaviour and hypersmooth behaviour. In each case we present analytical results pertaining to the continuum models and compare the predictions so obtained with the results obtained by numerical simulations of the corresponding discretised equations.

In general, the complexity of sandpile dynamics leads us to equations which are coupled, nonlinear and noisy: these equations present challenges to the theoretical physicist in more ways than the obvious ones to do with their detailed analysis and/or their numerical solutions. In particular, our analysis of Case C reveals the presence of hidden length scales whose existence was suspected analytically, but not demonstrated numerically in earlier work [5,14].

The normal procedure for probing temporal and spatial roughening in interface problems is to determine the asymptotic behaviour of the interfacial width with respect to time and space, via the single Fourier transform. Here only one of the variables, (x, t) is integrated over in Fourier space, and appropriate scaling relations are invoked to determine the critical exponents which govern this behaviour. However, it turns out that this leads to ambiguities for those classes of problems where there is an absence of simple scaling, or to be more specific, where multiple length scales exist. In such cases we demonstrate that the double Fourier transform (where *both* time and space are integrated over) yields insights that are harder to obtain via the single Fourier transform.

This point is illustrated by Case A, an exactly solvable model that we introduce; we then use it to understand Case C, a nonlinear model where our analytical results are clearly only approximations to the truth.

In order to make some of these ideas more concrete, we now review some general facts about rough interfaces [15]. Three critical exponents, α , β , and z , characterise the spatial and temporal scaling behaviour of a rough interface. They are conveniently defined by considering the (connected) two-point correlation function of the heights

$$S(x - x', t - t') = \langle h(x, t)h(x', t') \rangle - \langle h(x, t) \rangle \langle h(x', t') \rangle. \quad (1)$$

We have

$$S(x, 0) \sim |x|^{2\alpha} \quad (|x| \rightarrow \infty) \quad \text{and} \quad S(0, t) \sim |t|^{2\beta} \quad (|t| \rightarrow \infty),$$

and more generally

$$S(x, t) \approx |x|^{2\alpha} F(|t|/|x|^z)$$

in the whole long-distance scaling regime (x and t large). The scaling function F is universal in the usual sense; α and $z = \alpha/\beta$ are respectively referred to as the roughness exponent and the dynamical exponent of the problem. In addition, we have for the full structure factor which is the double Fourier transform $S(k, \omega)$

$$S(k, \omega) \sim \omega^{-1} k^{-1-2\alpha} \Phi(\omega/k^z)$$

which gives in the limit of small k and ω ,

$$S(k, \omega = 0) \sim k^{-1-2\alpha-z} \quad (k \rightarrow 0) \quad \text{and} \quad S(k = 0, \omega) \sim \omega^{-1-2\beta-1/z} \quad (\omega \rightarrow 0) \quad (2)$$

The scaling relations for the corresponding single Fourier transforms are

$$S(k, t = 0) \sim k^{-1-2\alpha} \quad (k \rightarrow 0) \quad \text{and} \quad S(x = 0, \omega) \sim \omega^{-1-2\beta} \quad (\omega \rightarrow 0) \quad (3)$$

In particular we note that the scaling relations for $S(k, \omega)$ (Eq.(2)) always involve the simultaneous presence of α and β , whereas those corresponding to $S(x, \omega)$ and $S(k, t)$ involve these exponents *individually*. Thus, in order to evaluate the double Fourier transforms, we need in each case information from the growing as well as the saturated interface (the former being necessary for β and the latter for α) whereas for the single Fourier transforms, we need only information from the saturated interface for $S(k, t = 0)$ and information from the growing interface for $S(x = 0, \omega)$. On the other hand, the information that we will get out of the double Fourier transform will provide a more unambiguous picture in the case where multiple length scales are present, something which cannot easily be obtained in every case with the single Fourier transform.

In Sections II, III and IV we present, analyse and discuss the results of Cases A, B and C respectively. Finally, in Section V, we reflect on the unifying features of these models, and make some educated guesses on the dynamical behaviour of real sandpile surfaces.

II. CASE A: THE EDWARDS-WILKINSON EQUATION WITH FLOW

Our first model involves a pair of linear coupled equations, where the equation governing the evolution of clusters (“stuck” grains) h is closely related to the very well-known Edwards-Wilkinson (EW) model [16]. The equations are:

$$\frac{\partial h(x, t)}{\partial t} = D_h \nabla^2 h(x, t) + c \nabla h(x, t) + \eta(x, t) \quad (4a)$$

$$\frac{\partial \rho(x, t)}{\partial t} = D_\rho \nabla^2 \rho(x, t) - c \nabla h(x, t) \quad (4b)$$

where the first of the equations describes the height $h(x, t)$ of the sandpile surface at (x, t) measured from some mean $\langle h \rangle$, and is precisely the EW equation in the presence of the flow term $c \nabla h$. The second equation describes the evolution of flowing grains, where $\rho(x, t)$ is the local density of such grains at any point (x, t) . As usual, the noise $\eta(x, t)$ is taken to be Gaussian so that:

$$\langle \eta(x, t) \eta(x', t') \rangle = \Delta^2 \delta(x - x') \delta(t - t').$$

with Δ the strength of the noise. Here, $\langle \dots \rangle$ refers to an average over space as well as over noise.

A. Analysis of the decoupled equation in h

For the purposes of analysis, we focus on the first of the two coupled equations (Eq.(4a)) presented above,

$$\frac{\partial h}{\partial t} = D_h \nabla^2 h + c \nabla h + \eta(x, t)$$

noting that this equation is essentially decoupled from the second. (This statement is, however, not true in reverse, which has implications to be discussed later). We note that this is entirely equivalent to the Edwards-Wilkinson equation [16] in a frame moving with velocity c

$$x' = x + ct, \quad t' = t$$

and would on these grounds expect to find only the well-known EW exponents $\alpha = 0.5$ and $\beta = 0.25$ [16]. This would be verified by naive single Fourier transform analysis of Eq.(4a) which yields these exponents via Eq.(3).

Equation (4a) can be solved exactly as follows. The propagator $G(k, \omega)$ is

$$G_h(k, \omega) = (-i\omega + D_h k^2 + ikc)^{-1}$$

This can be used to evaluate the structure factor

$$S_h(k, \omega) = \frac{\langle h(k, \omega) h(k', \omega') \rangle}{\delta(k + k') \delta(\omega + \omega')}$$

which is the Fourier transform of the full correlation function $S_h(x - x', t - t')$ defined by Eq.(1). The solution for $S_h(k, \omega)$ so obtained is:

$$S_h(k, \omega) = \frac{\Delta^2}{(\omega - ck)^2 + D_h^2 k^4} \quad (5)$$

This is illustrated in Fig.1 while representative graphs for $S_h(k, \omega = 0)$ and $S_h(k = 0, \omega)$ are presented in Figs.2 and 3 respectively. Before proceeding further, we make the following observation about the double Fourier transform $S_h(k = 0, \omega)$; this shows an ω^{-2} behaviour coming from Eq.(5), which we will also see later. We mention here that the ubiquity of this ω^{-2} arises from the form of the scaling relation Eq.(2), which is relevant for frequencies $\omega < \omega_c \approx k^{z_h}$, whereas for $\omega > \omega_c$ the high frequency behaviour takes over giving ω^{-2} (cf. Eq.(A2) in the Appendix). As $k = 0$ for the purposes of calculation of this structure factor, it is always the high frequency behaviour that dominates, leading to the ubiquity of ω^{-2} whenever it is measured.

It is obvious from Eq.(5) that $S_h(k, \omega)$ does not show simple scaling. More explicitly, if we write

$$S_h^{-1}(k, \omega = 0) = \frac{\omega_0^2}{\Delta^2} \left(\frac{k}{k_0} \right)^2 \left[1 + \left(\frac{k}{k_0} \right)^2 \right]$$

with $k_0 = c/D_h$, and $\omega_0 = c^2/D_h$, we see that there are two limiting cases :

- for $k \gg k_0$, $S_h^{-1}(k, \omega = 0) \sim k^4$; using again $S_h^{-1}(k = 0, \omega) \sim \omega^2$, we obtain $\alpha_h = 1/2$ and $\beta_h = 1/4$, $z_h = 2$ via Eqs.(2).
- for $k \ll k_0$, $S_h^{-1}(k, \omega = 0) \sim k^2$; using the fact that the limit $S_h^{-1}(k = 0, \omega)$ is always ω^2 , this is consistent with the set of exponents $\alpha_h = 0$, $\beta_h = 0$ and $z_h = 1$ via Eqs.(2).

The first of these contains no surprises, being the normal EW fixed point [16], while the second represents a new, ‘smoothing’ fixed point.

We now explain this smoothing fixed point via a simple physical picture. The competition between the two terms in Eq.(4a) determines the nature of the fixed point observed: when the diffusive term dominates the flow term, the canonical EW fixed point is obtained, in the limit of large wavevectors k . On the contrary, when the flow term predominates, the effect of diffusion is suppressed by that of a travelling wave whose net result is to penalise large slopes; this leads to the smoothing fixed point obtained in the case of small wavevectors k . We emphasise however, that this is a toy model of smoothing, which will be used to illuminate the discussion of models B and C below.

B. Coupled equations: a model of smoothing

We realise from the above that the interface h is smoothed because of the action of the flow term which penalises the sustenance of finite gradients ∇h in Eq.(4a). However, Eq.(4a) is effectively decoupled from Eq.(4b), while Eq.(4b) is manifestly coupled to Eq.(4a). In order for the coupled Eqs.(4) to qualify as a valid model of sandpile dynamics, we would need to ensure that no instabilities are generated in either of these by the coupling term $c\nabla h$.

In this spirit, we look first at the value of ρ averaged over the sandpile, as a function of time (Fig.6a). We observe that the incursions of $\langle \rho \rangle$ into negative values are limited to relatively small values, suggesting that the addition of a constant background of ρ exceeding this negative value would render the coupled system meaningful, at least to a first approximation. In order to ensure that this average does not involve wild fluctuations, we examine the fluctuations in ρ , viz. $\sqrt{\langle \rho^2 \rangle - \langle \rho \rangle^2}$ (Fig.6b). The trends in that figure indicate that this quantity appears to saturate, at least upto computationally accessible times. Finally we look at the *minimum* and *maximum* value of ρ at any point in the pile over a large range of times (Fig.6c); this appears to be bounded by a modest (negative) value of ‘bare’ ρ . Our conclusions are thus that the fluctuations in ρ saturate at computationally accessible times and that the negativity of the fluctuations in ρ can always be handled by starting with a constant ρ_0 , a constant ‘background’ of flowing grains, which is more positive than the largest negative fluctuation.

Physically, then, the above implies that at least in the presence of a constant large density ρ_0 of flowing grains, it is possible to induce the level of smoothing corresponding to the fixed point $\alpha = \beta = 0$. This model is thus one of the simplest possible ways in which one can obtain a representation of the smoothing of the ‘bare surface’ that is frequently observed in experiments on real sandpiles after intermittent avalanche propagation [9].

III. CASE B: A SIMPLE FORM OF COUPLING, WITH COMPLEX CONSEQUENCES

Our model equations, first presented in [5] involve a simple coupling between the species h and ρ , where the transfer between the species occurs only in the presence of the flowing grains and is therefore relevant to the regime of continuous avalanching when the duration of the avalanches is *large* compared to the time between them. The equations are:

$$\frac{\partial h(x, t)}{\partial t} = D_h \nabla^2 h(x, t) - T(h, \rho) + \eta_h(x, t) \quad (6a)$$

$$\frac{\partial \rho(x, t)}{\partial t} = D_\rho \nabla^2 \rho(x, t) + T(h, \rho) + \eta_\rho(x, t) \quad (6b)$$

$$T(h, \rho) = -\mu\rho(\nabla h) \quad (6c)$$

where the terms $\eta_h(x, t)$ and $\eta_\rho(x, t)$ represent Gaussian white noise as usual:

$$\begin{aligned} \langle \eta_h(x, t) \eta_h(x', t') \rangle &= \Delta_h^2 \delta(x - x') \delta(t - t') \\ \langle \eta_\rho(x, t) \eta_\rho(x', t') \rangle &= \Delta_\rho^2 \delta(x - x') \delta(t - t') \end{aligned}$$

and the $\langle \dots \rangle$ stands for average over space as well as noise.

A simple physical picture of the coupling or ‘transfer’ term $T(h, \rho)$ between h and ρ is the following: flowing grains are added in proportion to their local density to regions of the interface which are at less than the critical slope, and vice versa, *provided that the local density of flowing grains is always non-zero*. This form of interaction becomes zero in the absence of a finite density of flowing grains ρ (when the equations become decoupled) and is thus the simplest form appropriate to the situation of continuous avalanching in sandpiles. We analyse in the following the profiles of h and ρ consequent on this form.

It turns out that a singularity discovered by Edwards [18] three decades ago in the context of fluid turbulence is present in models with a particular form of the transfer term T ; the above is one example, while another example is the model due to Bouchaud *et al.* (BCRE) [7] where

$$T = -\nu \nabla h - \mu\rho(\nabla h)$$

and the noise is present only in the equation of motion for h . This singularity, the so-called infrared divergence, largely controls the dynamics and produces unexpected exponents.

A. Theoretical analysis

We carry out first the theoretical analysis of Eqs.(6). An examination of the above equations reveals the presence of two likely length scales in each, one associated with the diffusive motion, and the other with the so-called transfer term $T(h, \rho)$, representing the coupling between the two species. In these circumstances, a renormalisation group analysis would clearly be inappropriate due to the breakdown of simple scaling. In recent years, however, a self-consistent mode coupling analysis used hitherto in dynamic critical phenomena [19] has been used to look at in particular the Kardar-Parisi-Zhang (KPZ) equation [17,20] and we extend its use to the case of the coupled equations presented here.

In this method we set up equations (to one-loop order) for the correlation functions and self-energies in terms of the full Green’s functions, correlation functions and vertices using assumed scaling forms for each. The critical exponents α and β defined above are obtained from the self-consistent solutions of these equations using $D_h = D_\rho$.

Focusing on the h variable to start with, we define the Green’s functions and the correlation functions of the h and ρ variables

$$\begin{aligned} G_h(k, \omega) &= \left\langle \frac{\delta h(k, \omega)}{\delta \eta(k', \Omega)} \right\rangle \frac{1}{\delta(k + k') \delta(\omega + \Omega)} \\ G_\rho(k, \omega) &= \left\langle \frac{\delta \rho(k, \omega)}{\delta \eta(k', \Omega)} \right\rangle \frac{1}{\delta(k + k') \delta(\omega + \Omega)} \\ S_h(k, \omega) &= \frac{\langle h(k, \omega) h(k', \Omega) \rangle}{\delta(k + k') \delta(\omega + \Omega)} \\ S_\rho(k, \omega) &= \frac{\langle \rho(k, \omega) \rho(k', \Omega) \rangle}{\delta(k + k') \delta(\omega + \Omega)} \end{aligned}$$

The analysis of these functions will be in terms of a weak scaling hypothesis which states

$$G_h(k, \omega) = k^{-z_h} f_h\left(\frac{\omega}{k^{z_h}}, \frac{\omega}{k^{z_\rho}}\right)$$

$$G_\rho(k, \omega) = k^{-z_\rho} f_\rho\left(\frac{\omega}{k^{z_h}}, \frac{\omega}{k^{z_\rho}}\right)$$

A strong scaling would imply the existence of a single time scale *i.e.* $z_h = z_\rho$. As we show below, this cannot be the case here. The absence of strong scaling implies that the roughness exponents α_h and α_ρ may become functions of k .

We consider the full Green's function $G_h(k, \omega)$, which is given via the well-known Dyson equation [21] ,

$$G_h^{-1}(k, \omega) = G_h^{0-1}(k, \omega) + \Sigma_h(k, \omega)$$

Here, the zeroth order Green's function is

$$G_h^0(k, \omega) = (-i\omega + k^2)^{-1}$$

The scaling forms of the functions $G_h(k, \omega)$ and $S_h(k, \omega)$ are given by, in the limit $\omega \rightarrow 0$,

$$G_h(k, \omega) \sim \frac{1}{i\omega + k^2 + k^{z_h}}$$

$$S_h(k, \omega) \sim \frac{1}{k^{1+2\alpha_h-z_h}} \left(\frac{1}{\omega^2 + k^{2z_h}} \right)$$

Similar scaling relations hold for the species ρ .

To one-loop order, the self-energy $\Sigma_h(k)$ is given by (Fig.7b)

$$\Sigma_h(k, \omega) = \mu^2 \int \frac{dq}{2\pi} \int \frac{d\Omega}{2\pi} G_h(k-q, \omega-\Omega) S_\rho(q, \Omega) k(k-q) \quad (7a)$$

$$\sim \mu^2 \int \frac{dq}{2\pi} \int \frac{d\Omega}{2\pi} \left[\frac{1}{i(\omega-\Omega) + \Sigma_h(k-q, \omega-\Omega)} \right] \frac{k(k-q)}{q^{1+2\alpha_\rho}} \left[\frac{2\Sigma_\rho(q, \Omega)}{\Omega^2 + |\Sigma_\rho(q, \Omega)|^2} \right] \quad (7b)$$

where the second line follows from the first in the limit of small Ω . We note that due to the presence of the term $q^{-1-2\alpha_\rho}$, the integral is dominated by the singularity in the integrand at $q \rightarrow 0$. This 'infrared divergence' which results from the divergence of the *internal* momenta q , is very different from the usual divergences encountered in critical phenomena where the latter occur for small wave numbers and are associated with long wavelength instabilities in the external momenta. In this case due to the infrared divergence in the above equation in the internal momenta q , the integral diverges *for any value of the external momenta* k , so long as $\alpha_\rho > 0$.

We thus need either to evaluate the integral with a lower cut-off k_0 or to introduce a suitable regulator. We follow the first of these procedures for the above equation, and the second of the procedures to do with the corresponding quantity, $S_\rho(k, \omega)$, for ρ .

We then proceed to evaluate the self-energy at zero external frequency, *i.e.* $\Sigma_h(k, \omega = 0)$ from Eq.(7a). As $q \rightarrow 0$ we can approximate $G_h(k-q, -\Omega)$ by

$$G_h^{-1}(k, -\Omega) = i\Omega + k^2 + \Sigma_h(k, -\Omega)$$

$$\approx k^2 + \Sigma_h(k, 0)$$

where the second line follows from the fact that we are looking at the $q \simeq 0$ limit of the internal frequency $\Omega \sim q^{z_h}$. As $\Sigma_h(k, 0) \sim k^{z_h}$, the small k behaviour of $G_h(k)$ is dominated by $\Sigma_h(k)$ for $z_h < 2$, *i.e.*

$$G_h^{-1}(k) \sim \Sigma_h(k)$$

The integral in Eq.(7a) becomes in the limit of zero external frequencies

$$\Sigma_h(k) = \frac{\mu^2 k^2}{\Sigma_h(k)} \int \frac{dq}{2\pi} \int \frac{d\Omega}{2\pi} S_\rho(q, \Omega)$$

Using the scaling form for the single Fourier transform (Eq.(3)) we find

$$\Sigma_h(k) = \mu^2 k^2 \Sigma_h(k)^{-1} C_\rho \int \frac{dq}{2\pi} \frac{1}{q^{1+2\alpha_\rho}}$$

We now have to evaluate the integral by cutting off the momentum integration at $k_0 \ll 1$, *i.e.* we follow the first of the procedures given above to handle the infrared divergence. This gives, after some simplification,

$$\Sigma_h^2(k) = \mu^2 k^2 \frac{k_0^{-2\alpha_\rho} C_\rho}{4\pi\alpha_\rho}$$

From the above equation with the scaling relation $\Sigma_h(k) \sim k^{z_h}$ we find, on equating powers of k ,

$$z_h = 1$$

We note here that the presence of the term $\rho \nabla h$ could in principle cause the vertex μ to renormalise, leading to a correction to z_h . In these circumstances, the expression for the self-energy $\Sigma_h(k, \omega = 0)$ is given by

$$\Sigma_h(k, \omega = 0) = \mu^2 \int \frac{dq}{2\pi} \int \frac{d\Omega}{2\pi} \Gamma_3(k, q, k - q) G_h(k - q, -\Omega) S_\rho(q, \Omega) k(k - q) \quad (8)$$

where we have introduced a three-point vertex function $\Gamma_3(k, q, k - q)$ in Eq.(7a). Assuming that as $q \rightarrow 0$, we can write the asymptotic form for the three-point vertex as,

$$\Gamma_3(k, q, k - q) \sim k^{x_\mu} \quad (9)$$

we find

$$z_h = 1 + \frac{x_\mu}{2}$$

In the event that numerical results suggest $z_h \neq 1$ we will have to incorporate this new renormalised vertex into our calculations.

Next we examine the correlation function for h , $S_h(k, \omega)$, which to one-loop order is given by (Fig.8a)

$$S_h(k, \omega) = \frac{1}{\omega^2 + |\Sigma_h(k, \omega)|^2} \left[1 + \mu^2 \int \frac{dq}{2\pi} \int \frac{d\Omega}{2\pi} |k - q|^2 S_h(k - q, \omega - \Omega) S_\rho(q, \Omega) \right] \quad (10a)$$

$$\approx \frac{1}{\omega^2 + |\Sigma_h(k, \omega)|^2} \left[1 + \mu^2 \int \frac{dq}{2\pi} \int \frac{d\Omega}{2\pi} \frac{|k - q|^2}{|k - q|^{1+2\alpha_h}} \frac{1}{q^{1+2\alpha_\rho}} \left(\frac{2\Sigma_\rho(q, \Omega)}{\Omega^2 + |\Sigma_\rho(q, \Omega)|^2} \right) \left(\frac{2\Sigma_h(k - q, \omega - \Omega)}{(\omega - \Omega)^2 + |\Sigma_h(k - q, \omega - \Omega)|^2} \right) \right] \quad (10b)$$

$$\approx \frac{1}{\omega^2 + |\Sigma_h(k, \omega)|^2} \left[1 + \mu^2 \int \frac{dq}{2\pi} \frac{|k - q|^{1-2\alpha_h}}{q^{1+2\alpha_\rho}} \left(\frac{\Sigma_\rho(q) + \Sigma_h(k - q)}{\omega^2 + (\Sigma_\rho(q) + \Sigma_h(k - q))^2} \right) \right] \quad (10c)$$

The frequency-dependent self-energy $\Sigma_h(k, \omega)$ in the above is given by evaluating the integral over the internal frequency Ω in Eq.(7b). This leads to

$$\Sigma_h(k, \omega) \approx \mu^2 \int \frac{dq}{2\pi} \frac{k(k - q)}{q^{1+2\alpha_\rho}} \frac{A}{-i\omega + \Sigma_\rho(q) + \Sigma_h(k - q)} \quad (11a)$$

$$\approx \mu^2 \frac{A}{4\pi\alpha_\rho} \frac{k^2 k_0^{-2\alpha_\rho}}{-i\omega + \Gamma_0 k} \quad (11b)$$

$$\approx \frac{\Gamma_0^2 k^2}{-i\omega + \Gamma_0 k} \quad (11c)$$

where $\Gamma_0 = \mu k_0^{-\alpha_\rho} \sqrt{\frac{A}{4\pi\alpha_\rho}}$, and the second line in the above follows from taking a $q \rightarrow 0$ limit and introducing a cutoff wavevector k_0 in the integral on the first line. Introducing this expression for $\Sigma_h(k, \omega)$ in Eq.(10c) and recognising that the divergence due to $q^{-(1+2\alpha_\rho)}$ dominates the integral we find

$$S_h(k, \omega) = \left(\omega^2 + \frac{\Gamma_0^4 k^4}{\omega^2 + \Gamma_0^2 k^2} \right)^{-1} \left[1 + \frac{\mu^2 C_\rho}{4\pi\alpha_\rho} k_0^{-2\alpha_\rho} \frac{k^2}{k^{1+2\alpha_h}} \frac{\Gamma_0 k}{\omega^2 + \Gamma_0^2 k^2} \right] \quad (12)$$

On integrating with respect to ω we can write the structure factor $S_h(k, t = 0)$ as

$$S_h(k, t=0) \equiv \int S_h(k, \omega) \frac{d\omega}{2\pi} = \frac{A_0}{k} + \frac{B_0}{k^{1+2\alpha_h}} \quad (13)$$

Recognising that the scaling form of $S_h(k, t=0) \sim k^{-1-2\alpha_h}$, we notice that α_h cannot in general be determined from Eq.(13). This is because the second term on the right-hand-side of Eq.(13) dominates at small momenta k provided $\alpha_h > 0$, indicating that α_h is indeterminate to this order of calculation.

We turn now to the critical exponents in ρ . The single loop self-energy $\Sigma_\rho(k, \omega)$ is given as shown in Fig.7a by

$$\Sigma_\rho(k, \omega=0) = -\mu^2 \int \frac{dq}{2\pi} \int \frac{d\Omega}{2\pi} G_\rho(k-q, -\Omega) S_h(q, \Omega) q^2 \quad (14)$$

Inserting the expressions for $G_\rho(k-q, \omega-\Omega)$ and $S_h(q, \Omega)$ we find

$$\Sigma_\rho(k, \omega=0) = -\mu^2 \int \frac{dq}{2\pi} \int \frac{d\Omega}{2\pi} \left[\frac{1}{i\Omega + |k-q|^{z_\rho}} \right] \left[\frac{2q^{z_h}}{\Omega^2 + q^{2z_h}} \right] \frac{q^2}{q^{1+2\alpha_h}}$$

This gives, on performing the integral over internal frequency Ω ,

$$\Sigma_\rho(k, \omega=0) = -\mu^2 \int \frac{dq}{2\pi} \frac{q^2}{q^{1+2\alpha_h}} \frac{1}{|k-q|^{z_\rho} + q^{z_h}}$$

In order to discuss this further in the context of z_ρ , we need to make a statement about α_h and z_h . We have already obtained $z_h = 1$ in the foregoing and will now quote our numerical result for α_h , viz. $\alpha_h = 0.5$. For small k the self-energy can then be written as

$$\Sigma_\rho(k, \omega) \simeq -\mu^2 \left[\int \frac{dq}{2\pi} \frac{1}{(q + q^{z_\rho})} + z_\rho k \int \frac{dq}{2\pi} \frac{1}{(q + q^{z_\rho})(q + q^{2z_\rho})} \right]$$

We see from the above that $\Sigma_\rho(k, 0)$, the relaxation rate for ρ fluctuations, is negative and finite as $k \rightarrow 0$, and we need to add a positive constant, Σ_0 , to the self-energy ($\Sigma_0 > |\Sigma_\rho(k \rightarrow 0)|$) for regulatory purposes. This divergence in the relaxation rate, needing regulation, is reflected in the divergence we have encountered in our numerical investigations below; we have there followed an analogous procedure by introducing a numerical regulator which replaces divergent values of the transfer term by suitably defined cutoffs [5]. The resulting constancy of Σ_ρ implies $z_\rho \approx 0$ for the regulated equations and will be used in the following.

The correlation function $S_\rho(k, \omega)$ is given by (Fig.8b)

$$S_\rho(k, \omega) = \frac{1}{(\omega^2 + k^{2z_\rho})} \int \frac{dq}{2\pi} \int \frac{d\Omega}{2\pi} (k-q)^2 S_h(k-q, \omega-\Omega) S_\rho(q, \Omega)$$

The above integral will now be evaluated in the limit $q \rightarrow 0$ and since $\Omega \sim q^{z_h}$ for S_h we can replace

$$S_h(k-q, \omega-\Omega) \simeq S_h(k, \omega).$$

Then using the scaling relation Eq.(3) we have

$$S_\rho(k, \omega) \simeq \frac{1}{(\omega^2 + k^{2z_\rho})} \int \frac{dq}{2\pi} \frac{C_\rho}{q^{1+2\alpha_\rho}} k^2 S_h(k, \omega) \quad (15a)$$

$$= \frac{k^2 C_\rho}{(\omega^2 + k^{2z_\rho})} S_h(k, \omega) \int \frac{dq}{2\pi} \frac{1}{q^{1+2\alpha_\rho}} \quad (15b)$$

$$= \frac{C_\rho k_0^{-2\alpha_\rho}}{4\pi\alpha_\rho} \frac{k^{1-2\alpha_h+z_h}}{(\omega^2 + k^{2z_\rho})(\omega^2 + k^{2z_h})} \quad (15c)$$

where the last step follows from introducing a lower cutoff k_0 in the momentum integration over q .

Using Eq.(3) we have after integrating Eq.(15c) over ω

$$S_\rho(k, t=0) \sim k^{-(1+2\alpha_\rho)} \sim \frac{k^{1-2\alpha_h}}{k^{z_\rho}(k^{z_h} + k^{z_\rho})} \quad (16)$$

Finally using $z_\rho \approx 0$ we have

$$\alpha_\rho = \alpha_h + \frac{z_h}{2} - 1 \quad \text{for large } k \quad (17a)$$

$$\alpha_\rho = \alpha_h - 1 \quad \text{for small } k \quad (17b)$$

Given our numerical result of $\alpha_h = 0.5$, the above predicts a negative α_ρ , at small k . This is consistent with, and validates our assumption of, a cutoff k_0 which arises naturally as the wavevector separating the region of $\alpha_\rho < 0$ (no infrared divergence) and $\alpha_\rho > 0$ (infrared divergence prevalent) in Eqs.(7b) and (10c).

More importantly, this non-trivial result for α_ρ indicates that should we see numerical evidence of a negative α_ρ for small wavevectors, we will have verified the existence of an asymptotic hypersmoothing in our model equations, which has an important bearing on sandpile surfaces in the continuous avalanching regime. This is discussed further in our concluding section.

B. Numerical Analysis

We focus now on our numerical results for Case B. The coupled equations in this section and the following one were numerically integrated by using the method of finite differences [22]. Our grids in time and space were kept as fine-grained as computational constraints allowed so that our grid size in space Δx was chosen to be in the range (0.1, 0.5) whereas that in time was in the range Δt (0.001, 0.005). Thus the instabilities associated with the discretisation of nonlinear continuum equations were avoided and convergence was checked by keeping Δt small enough such that the quantities under investigation were independent of further discretisation. Our results were also checked for finite size effects. In the calculations of this section we chose $D_h = D_\rho = 1.0$ and $\mu = 1$ and our results were averaged over several independent configurations. We have calculated the exponents α and β and the corresponding error bars using the linear least square fit so that $-(1 + 2\beta)$ and $-(1 + 2\alpha)$ are given by slopes of the fitted straight lines.

On discretising the equations Eqs.(6) we found once again the divergences that were previously observed in [5]. These divergences are in our view a direct representation of the infrared divergence mentioned above, and we follow here a parallel course in regulating these via an explicit regulator. In earlier work [5], a regulator was introduced which replaced the function $\mu\rho\nabla h$ by the following:

$$\begin{aligned} T &= +1 && \text{for } \mu\rho(\nabla h) > 1 \\ &= \mu\rho(\nabla h) && \text{for } -1 \leq \mu\rho(\nabla h) \leq 1 \\ &= -1 && \text{for } \mu\rho(\nabla h) < -1 \end{aligned}$$

In addition in this paper, we have introduced noise reduction to the regulated equations which has led to a more accurate evaluation of all our critical exponents.

The Fourier transform $S_h(k, t = 0)$ (Fig.9) is consistent with a spatial roughening exponent $\alpha_h \sim 0.501 \pm 0.007$ via our observation of

$$S_h(k, t = 0) \sim k^{-2.03 \pm 0.014}$$

and the Fourier transform $S_h(x = 0, \omega)$ (Fig.10) is consistent with a temporal roughening exponent $\beta_h \sim 0.465 \pm 0.008$ via our observation of

$$S_h(x = 0, \omega) \sim \omega^{-1.93 \pm 0.017}$$

Hence $z_h \sim 1.07$, and thus the exponent $x_\mu \simeq 0$ (Eq.(9)), indicating that the μ vertex does not renormalise.

Using $\alpha_h \sim 0.5$ in Eq.(12) we can write the structure factor $S_h(k, \omega)$ as

$$S_h(k, \omega) = \frac{1}{1 + \Omega^2(1 + \Omega^2)} \left[\frac{1 + \Omega^2}{\Gamma_0^2 k^2} + \frac{1}{\Gamma_0 k^3} \right] \quad (18)$$

where $\Omega = \omega/\Gamma_0 k$. We find from the above that the expected form of $S_h(k, \omega = 0)$ in the limit of small wavevectors to be

$$S_h(k, \omega = 0) \sim k^{-3} \quad (19)$$

Realising that our computed $\alpha_h < 1$, we obtain from Eq.(12) the prediction

$$S_h(k = 0, \omega) \sim \omega^{-2} \quad (20)$$

The full structure factor $S_h(k, \omega)$ has been calculated at two different k points and Fig.11 displays our results to Eq.(18). The solid and the dashed line in the Fig.11 are the plots of the Eq.(18) for $k = 0.1$ and $k = 0.2$ with $\Gamma_0 = 0.4$ and 0.5 respectively. The spatial structure factor $S_h(k, \omega = 0)$ shows a power-law behaviour (Fig.12) given by

$$S_h(k, \omega = 0) \sim k^{-3.40 \pm 0.029}$$

in qualitative accord with Eq.(19), and the temporal structure factor $S_h(k = 0, \omega)$ shows a power-law behaviour (Fig.13) given by

$$S_h(k = 0, \omega) \sim \omega^{-1.91 \pm 0.017}$$

in accord with Eq.(20).

Given our values of $\alpha_h \simeq 0.5$ and $z_h \simeq 1$, Eqs.(17a) and (17b) predict a crossover in α_ρ from 0 at large k to -0.5 as $k \rightarrow 0$. The single Fourier transform $S_\rho(k, t = 0)$ (Fig.15) shows a crossover behaviour from

$$S_\rho(k, t = 0) \sim k^{-2.12 \pm 0.017}$$

for large wavevectors to

$$S_\rho(k, t = 0) \sim \text{constant}$$

as $k \rightarrow 0$. In Fig.15 we find a crossover from 0.56 at large k to -0.5 as $k \rightarrow 0$, which shows the same trend as the prediction above. Note however that the simulations also manifest in addition to the above the normal diffusive behaviour represented by $\alpha_\rho = 0.56$ at large wavevectors. The single Fourier transform in time $S_\rho(x = 0, \omega)$ (Fig.14) shows a power-law behaviour

$$S_\rho(x = 0, \omega) \sim \omega^{-1.81 \pm 0.017}$$

While the range of wavevectors in Fig.15 over which crossover in $S_\rho(k, t = 0)$ is observed was restricted by our computational constraints, the form of the crossover appears conclusive. Checks (with fewer averages) over larger system sizes revealed the same trend; additionally our theoretical calculations support the observed crossover via Eqs. (17).

C. Homing in on the physics: a discussion of smoothing

We focus in this section on the physics of the equations and our results. In the regime of continuous avalanching in sandpiles, the major dynamical mechanism is that of mobile grains ρ present in avalanches flowing into voids in the h landscape as well as the converse process of unstable clusters (a surfeit of ∇h above some critical value) becoming destabilised and adding to the avalanches. Our results for the critical exponents in h indicate no further spatial smoothing beyond the diffusive; however, those in the species ρ indicate a crossover from purely diffusive to an asymptotic hypersmooth behaviour. Our claim for continuous avalanching is as follows: *the flowing grains play the major dynamical role as all exchange between h and ρ takes place only in the presence of ρ . These flowing grains therefore distribute themselves over the surface filling in voids in proportion both to their local density as well as to the depth of the local voids; it is this distribution process that leads in the end to a strongly smoothed profile in ρ .* Additionally, since in the regime of continuous avalanches, the effective interface is defined by the profile of the *flowing* grains, it is this profile that will be measured experimentally for, say, a rotating cylinder with high velocity of rotation.

IV. ANOMALOUS SMOOTHING: THE CASE OF TILT AND BOUNDARY-LAYER EXCHANGE (CASE C)

The last case we discuss in this paper involves a more complex coupling between the the stuck grains h and the flowing grains ρ as follows

$$\frac{\partial h(x, t)}{\partial t} = D_h \nabla^2 h(x, t) - T + \eta(x, t) \quad (21a)$$

$$\frac{\partial \rho(x, t)}{\partial t} = D_\rho \nabla^2 \rho(x, t) + T \quad (21b)$$

$$T(h, \rho) = -\nu(\nabla h)_- - \lambda \rho(\nabla h)_+ \quad (21c)$$

with $\eta(x, t)$ representing white noise as usual.

Here,

$$\begin{aligned} z_+ &= z & \text{for } z > 0 \\ &= 0 & \text{otherwise} \end{aligned} \tag{22a}$$

$$\begin{aligned} z_- &= z & \text{for } z < 0 \\ &= 0 & \text{otherwise} \end{aligned} \tag{22b}$$

This equation was also presented in earlier work [5] in the context of the surface dynamics of an evolving sandpile. The two terms in the transfer term T represent two different physical effects which we will discuss in turn. The first term represents the effect of tilt, in that it models the transfer of particles from the boundary layer at the ‘stuck’ interface to the flowing species whenever the local slope is steeper than some threshold (in this case zero, so that negative slopes are penalised). The second term is restorative in its effect, in that in the presence of ‘dips’ in the interface (regions where the slope is shallower, *i.e.* more positive than the zero threshold used in these equations), the flowing grains have a chance to resettle on the surface and replenish the boundary layer [2]. We notice that because one of the terms in T is independent of ρ we are no longer restricted to a coupling which exists only in the presence of flowing grains: *i.e.* this model is applicable to intermittent avalanches when ρ may or may not always exist on the surface. In the following we examine the effect of this interaction on the profiles of h and ρ respectively.

The complexity of the transfer term with its discontinuous functions precludes any attempts to solve this model along the lines of the earlier ones. We make some remarks here, however, on the likely critical behaviour of this model.

We observe that the transfer term

$$T = -\lambda\rho(\nabla h)_+ - \nu(\nabla h)_-$$

can be thought of as a formal infinite series by invoking a suitable representation for the Heaviside step functions in Eq.(23). We are then led to consider the following more general structure for the transfer term T ,

$$T = -\lambda\rho(\nabla h) - \nu(\nabla h) - \sum_{n=1}^{\infty} \nu_n(\nabla h)^{n+1} - \rho \sum_{n=1}^{\infty} \lambda_n(\nabla h)^{n+1} \tag{23}$$

Note however that this is not a very well-defined expansion because the coefficients in the infinite series could well be very large, if not infinite. However, given this disclaimer, we can still make the following comments in the spirit of self-consistency *i.e.* subject to numerical verification.

If $\lambda\rho(\nabla h)$ were the only nonlinearity, as in Case B, we would have $z_h = 1$. Using $h \sim x^{\alpha_h}$ and $\rho \sim x^{\alpha_\rho}$, we see $\lambda\rho(\nabla h)$ is a more relevant nonlinearity than $\nu_1(\nabla h)^2$, the leading nonlinear term in the expansion of $(\nabla h)_-$, and is likely to be the controlling nonlinearity for the extreme long wavelength behaviour. Fig.16 shows that the λ vertex never renormalises in the presence of the the KPZ term $\nu_1(\nabla h)^2$, so that z_h is always fixed at unity. However, the KPZ vertex corresponding to $\nu_1(\nabla h)^2$ has distinct behaviour in different wavevector ranges. In the range where the vertex renormalises, we cannot say much about the behaviour of α_h ; however, in the range where it does *not* renormalise, we might imagine that normal KPZ hyperscaling $\alpha_h + z_h = 2$ would be restored. This, with $z_h = 1$, would give $\alpha_h = 1$.

If $z_h = 1$, we can write the scaling relation $S_h(k, \omega = 0)$ for the double Fourier transform at zero frequency as

$$S_h(k, \omega = 0) \sim k^{-2-2\alpha_h}$$

which, in the regime where the KPZ hyperscaling holds, should look like $S_h(k, \omega = 0) \sim k^{-4}$.

We now try to obtain additional insights into the behaviour of these equations using the Hartree-Fock approximation. The spirit of Hartree-Fock is to replace nonlinear terms by linear ones with coefficients that are generally determined self-consistently. To undertake that here, we note that the step functions (Eq.23) give rise to nonlinearities and hence the simplest thing to do is to replace them by an expectation value (the argument of the step function is a random variable and hence this is an acceptable approximation). We represent this expectation value by a number c with $0 < c < 1$. The equations of motion thus read

$$\frac{\partial h}{\partial t} = D_h \nabla^2 h - \lambda' \rho \nabla h - \nu' \nabla h + \eta_h(x, t) \tag{24a}$$

$$\frac{\partial \rho}{\partial t} = D_\rho \nabla^2 \rho + \lambda' \rho \nabla h + \nu' \nabla h \tag{24b}$$

with $\lambda' = c\lambda$ and $\nu' = (1 - c)\nu$ and are identical to the ones studied by Bouchaud *et al.* [7]. We expect at least in some regime of Eqs.(21) to reproduce the mean-field results appropriate to Eqs.(24a,24b).

1. Results for the single Fourier transforms

The single Fourier transforms $S_h(k, t = 0)$ (Fig.17) and $S_h(x = 0, \omega)$ (Fig.18) show power-law behaviour corresponding to

$$S_h(k, t = 0) \sim k^{-2.56 \pm 0.060}$$

$$S_h(x = 0, \omega) \sim \omega^{-1.68 \pm 0.011}$$

which implies that the roughness and the growth exponents are given by respectively $\alpha_h = 0.78 \pm 0.030$ and $\beta_h = 0.34 \pm 0.005$. This suggests $z_h = \alpha_h/\beta_h \approx 2$ contradicting the prediction of $z_h = 1$ by perturbative methods and suggesting that the mean-field approach outlined in the above might be more appropriate. We discuss this further in what follows.

However, the small k limit of $S_h(k, t = 0)$ indicates a downward curvature and thus a deviation from the linear behaviour at higher k (Fig.17). This curvature, which had also been observed in previous work [5], indicates a smaller roughness exponent α_h there, *i.e.* an asymptotic *smoothing*.

2. Results for the double Fourier transforms

The double Fourier transforms $S_h(k, \omega = 0)$ (Fig.19) and $S_h(k = 0, \omega)$ (Fig.20) show power-law behaviour corresponding to

$$\begin{aligned} S_h(k = 0, \omega) &\sim \omega^{-1.80 \pm 0.007} \\ S_h(k, \omega = 0) &\sim k^{-4.54 \pm 0.081} \quad \text{for large wavevectors} \\ &\sim \text{constant} \quad \text{for small wavevectors} \end{aligned}$$

The double Fourier transform $S_h(k = 0, \omega)$ shows the usual ω^{-2} behaviour that we have seen before in Eqs.(5) and (20) which we have already discussed earlier.

The structure factor $S_h(k, \omega = 0)$ signals a dramatic behaviour of the roughening exponent α_h , which crosses over from

- A value of 1.3 indicating anomalously large roughening at intermediate wavevectors, to
- A value of about -1 for small wavevectors indicating asymptotic hypersmoothing.

The anomalous roughening $\alpha_h = 1$ seen here is consistent with that observed via the single Fourier transform (Fig.17) and suggests, via the perturbative arguments given previously, that $z_h = 1$. However, if we assume $z_h = 2$ according to the results of the single Fourier transforms given above, this would lead to an α_h of about 0.8, in agreement with the values obtained both via single Fourier transforms in the present paper, and in [5]. In either case, our values of α_h (either 1.3 or 0.8) suggest anomalous roughening of the interface at moderately large wavevectors.

The anomalous smoothing obtained here ($\alpha_h \sim -1$ if $z_h \sim 1$, and $\alpha_h \sim -1.5$ in the event that z_h is taken to be 2) is also consistent with the downward curvature in the single Fourier transform $S_h(k, t = 0)$, as both imply a negative α_h ; we mention also that the wavevector regime where this smoothing is manifested is almost identical in both Figs.17 and 19.

Since we expect that the anomalous smoothing results from a failure of the expansion of the step functions along the lines of Eq.(23), this underlines our expectation that the mean-field solution of Eqs.(24a,24b) would capture at least some of the flavour of this regime. We have therefore solved the mean-field equations (Eqs.24a,24b) numerically, and from Fig.22 and Fig.23 we find that there is a crossover in $S_h(k, t = 0)$ (Fig.22) from a diffusive behaviour ($z_h = 2$) at high wavevectors to a smoothing behaviour at low wavevectors.

This behaviour is reflected in our results for Case C. At low frequencies the region of anomalous smoothing can be understood by comparison with the corresponding region in the mean-field equations Eqs.(24a,24b) which also manifest this. At large k , $S_h(k, t = 0)$ and $S_h(k, \omega = 0)$ indicate anomalous roughening with $\alpha_h \approx z_h \approx 1$ which is consistent with the infrared divergence discussed in the previous section. However, as in Case A, $S_h(x = 0, \omega)$ is dominated by the diffusive $z_h = 2$ arising from the presence of $\delta(\omega - \nu'k)$ in the mean-field solution of Case C. This behaviour is corroborated by an evaluation of the full structure factor $S(k_i, \omega)$ (Fig.21) which shows a distinct peak at an ω_i given by $\omega_i = \nu'k_i$; this is reminiscent of the Lorentzian obtained in Case A (Fig.1). In fact, to leading order, $S_h(k, \omega)$ can be fitted to a Lorentzian; however, as we reduce the relative strength of $\nu(\nabla h)_-$ with respect

to $\lambda\rho(\nabla h)_+$ the Lorentzian peaks disappear, and we begin to see a ‘shoulder’ reminiscent, as it should be, of the behaviour observed in Case B (Fig.11). This suggests that the present model is an integrated version of the earlier two, reducing to their behaviour in different wavevector regimes; we speculate therefore that there are *two* dynamical exponents ($z_h = 1$ and $z_h = 2$) in the problem.

V. DISCUSSION AND CONCLUSIONS

We have presented in the above a discussion of three models of sandpiles, all of which manifest asymptotic smoothing: Cases A and C manifest this in the species h of stuck grains, while Case B manifests this in the species ρ of flowing grains. We reiterate that the fundamental physical reason for this is the following: Cases A and C both contain couplings which are independent of the density ρ of flowing grains, and are thus applicable for instance to the dynamical regime of intermittent avalanching in sandpiles, when grains occasionally but not always flow across the ‘bare’ surface. In Case B, by contrast, the equations are coupled only when there is continuous avalanching, *i.e.* in the presence of a finite density ρ of flowing grains.

The analysis of Case A is straightforward, and was undertaken really only to explain features of the more complex Case C; that of Case B shows satisfactory agreement between perturbative analysis and simulations. Anomalies persist however when such a comparison is made in Case C, because the discontinuous nature of the transfer term makes it analytically intractable. These are removed when the analysis includes a mean-field solution which is able to reproduce the asymptotic smoothing observed.

We suggest therefore an experiment where the critical roughening exponents of a sandpile surface are measured in

1. a rapidly rotated cylinder, in which the time between avalanches is much less than the avalanche duration. Our results predict that for small system sizes we will see only diffusive smoothing, but that for large enough systems, we will see extremely smooth surfaces.
2. a slowly rotated cylinder where the time between avalanches is much more than the avalanche duration. In this regime, the results of Case C make a fascinating prediction: anomalously large spatial roughening for moderate system sizes crossing over to an anomalously large spatial smoothing for large systems.

Finally we make some speculations in this context concerning natural phenomena. The qualitative behaviour of blown sand dunes [23] is in accord with the results of Case B, because sand moves swiftly and virtually continuously across their surface in the presence of wind. By contrast, on the surface of a glacier, we might expect the sluggish motion of boulders to result in intermittent flow across the surface, making the results of Case C more applicable to this situation. It would be interesting to see if the predictions of anomalous roughening at moderate, and anomalous smoothing at large, length scales is applicable here.

ACKNOWLEDGEMENTS

Parthapratim Biswas would like to thank the Council of Scientific and Industrial Research (CSIR) for financial assistance. Arnab Majumdar acknowledges the hospitality of SNBNCBS during the course of this work. Anita Mehta acknowledges the support of the National Science Foundation, under Grant no. PHY94-07194, at the Institute of Theoretical Physics, Santa Barbara, where part of this research was carried out. We thank the referee for a critical and careful reading of the manuscript.

-
- [1] H.M. Jaeger and S.R. Nagel, *Science* **255**, 1523 (1992); H.M. Jaeger, S.R. Nagel and R.P. Behringer, *Rev. Mod. Phys.* **68**, 1259 (1996); Anita Mehta and G.C. Barker, *Rep. Prog. Phys.* **57**, 383 (1994); D. Bideau and A. Hansen, Eds., *Disorder and Granular Media*, Random Materials and Processes Series, (North Holland. New York, 1993).
 - [2] *Granular Matter: An Interdisciplinary Approach*, ed. Anita Mehta (Springer Verlag, New York, 1993).
 - [3] P. Bak, C. Tang, and K. Wiesenfeld, *Phys. Rev. Lett.* **59**, 381 (1987); *Phys. Rev. A* **38**, 364 (1988).
 - [4] Anita Mehta and G.C. Barker, *Europhys. Lett.* **27**, 501 (1994).
 - [5] Anita Mehta, J.M. Luck, and R.J. Needs, *Phys. Rev. E* **53**, 92 (1996).
 - [6] Anita Mehta, R.J. Needs, and S. Dattagupta, *J. Stat. Phys.*, **68**, 1131 (1992).

- [7] J.P.Bouchaud, M.E.Cates, J.Ravi Prakash, and S.F.Edwards, J. Phys. I France **4**, 1383 (1994); Phys. Rev. Lett. **74**, 1982 (1995).
- [8] Anita Mehta and G.C.Barker, Phys. Rev. Lett. **67**, 394 (1991).
- [9] S.R.Nagel, private communication.
- [10] P.G.de Gennes, C. R. Acad. Sci. (Paris) **321**, 501 (1995); *Dynamique Superficielle d'un materiau granulaire*, submitted to Physique des Surfaces et des Interfaces.
- [11] R.Franklin and F.Johanson, Chem. Eng. Sci. **4**, 119 (1955).
- [12] H.M.Jaeger, C.H.Liu, S.R.Nagel, Phys. Rev. Lett. **62**, 40 (1989); P.Evesque, J.Rajchenbach, Phys. Rev. Lett.**62** 44 (1989); S.Douady, S.Fauve, C.Laroche, Europhys Lett.**8**, 621 (1989); G.A.Held et al, Phys. Rev. Lett. **65**, 1120 (1990); S.K.Grumbacher et al, Am. J. Phys. **61**, 329 (1993).
- [13] S.R. Nagel, Rev. Mod. Phys.**64**, 321 (1992).
- [14] Anita Mehta, J.K.Bhattacharjee and J.M.Luck, Pramana, **48**,749 (1996).
- [15] T.Halpin-Healy and Y.C.Zhang, Phys. Rep. **254**, 215 (1995); J.Krug and H.Spohn, in *Solids far from Equilibrium*, ed.C. Godr che (Cambridge University Press,1992).
- [16] S.F.Edwards and D.R.Wilkinson, Proc. Roy. Soc. London **A 381**, 17 (1982).
- [17] M.Kardar, G.Parisi, and Y.Zhang, Phys. Rev. Lett. **56**, 889 (1986).
- [18] S.F.Edwards, J. Fluid Mech. **18**, 239 (1964).
- [19] K. Kawasaki et al., Ann. Phys. (N.Y) **61**, 1 (1970).
- [20] J.P. Doherty, M.A.Moore, J.M.Kim and A.J. Bray, Phys. Rev. Lett. **72**, 2041 (1994).
- [21] G.D. Mahan, *Many-Particle Physics* (Plenum, New York, 1981).
- [22] C.W.Gear, Math. Comput. **21**, 146 (1967); *Numerical Initial value Problems in Ordinary Differential Equations* (Prentice Hall, 1971).
- [23] R.A. Bagnold, Proc. R. Soc. **A 225**,49 (1954); R.A. Bagnold, Proc. R. Soc. **A 295**,219 (1966).

APPENDIX:

In this appendix we discuss some of the technical points related with the double Fourier transform. We have found that the crossover that we have seen in the Eq.(5) would not have been observed had we been using the single Fourier transforms $S_h(k, t = 0)$ and $S_h(x = 0, \omega)$ for numerical purposes. We illustrate this by writing explicitly the expressions for the relevant quantities:

$$S_h(k, t = 0) \sim k^{-2} \quad (A1a)$$

$$S_h(x = 0, \omega) \sim \omega^{-2} \quad \text{for } \omega \text{ small} \quad (A1b)$$

$$S_h(x = 0, \omega) \sim \omega^{-1.5} \quad \text{for } \omega \text{ large} \quad (A1c)$$

The examination of $S_h(k, t = 0)$ (Fig.4) on its own yields no indication of the crossover to the smoothing fixed point; although there is a crossover in the $S_h(x = 0, \omega)$ graph (Fig.5a) from $\omega^{-1.5}$ to ω^{-2} , the analysis below shows that *both* regimes reflect diffusive behaviour, so that the smoothing fixed point ($\alpha_h = 0, \beta_h = 0, z_h = 1$) is entirely suppressed.

The single Fourier transform $S_h(x, \omega)$ is defined by

$$S_h(x = 0, \omega) = \int_{-\infty}^{\infty} \frac{dk}{2\pi} S_h(k, \omega) = \int_{-\infty}^{\infty} \frac{dk}{2\pi} \frac{1}{D_h k^{z_h}} \left[\frac{D_h k^{z_h}}{(\omega - ck)^2 + D_h^2 k^{2z_h}} \right]$$

In the limit $\omega \rightarrow ck$ the term in the square brackets behaves like a δ -function and thus

$$S_h(x = 0, \omega) = \int_{-\infty}^{\infty} \frac{dk}{2\pi} \frac{1}{D_h k^{z_h}} \delta(\omega - ck) \approx \frac{1}{\omega^{z_h}} \quad (A2)$$

This is the origin of ballistic behaviour in the flow term and is responsible for two anomalies.

1. Firstly, we notice from the above that the δ -function causes $S_h(x = 0, \omega)$ to behave like ω^{-z_h} . Comparing with Eq.(A1b) this leads to $z_h = 2$. However a simple-minded application of Eqs.(3) would have led to the *wrong* conclusion of $\beta_h = 0.5$. Even if the correct scaling relation Eq.(A2) were employed, the ballistic nature of the flow term picks out, misleadingly, the *high* frequency (diffusive) dynamical exponent in the *low* frequency regime of $S_h(x = 0, \omega)$ (Eq.(A1b)). The low wavevector, low-frequency smoothing behaviour is thus entirely suppressed.
2. Secondly, spurious oscillations are observed (Fig.5(b)) in the graph for $S_h(x = 0, \omega)$ as a function of grid size. A consideration of the form of the structure factor $S_h(x = 0, \omega)$ makes it clear the crossover from small to large ω should not involve any imaginary quantities, and therefore strictly speaking we should not see any oscillatory behaviour in the structure factor in this limit. However the full form of the structure factor $S_h(x, \omega)$ for finite x *does*

contain imaginary portions, which are responsible for the oscillations. The characteristic length and time scales in our problem are given by

$$t_0 = D_h/c^2 \quad x_0 = D_h/c$$

Whenever grid sizes in time or space are comparable to these characteristic lengths, the profile fluctuates across these intervals, which is then aggravated by the shock fronts associated with the flow term. This results in oscillatory behaviour arising from the *non-zero* intervals in x associated with the sampling of the profile to generate the Fourier transform, $S_h(x=0, \omega)$, which introduce a flavour of $S_h(x, \omega)$ for *finite* x . These become increasingly violent as c increases because of the increased fluctuations associated with the ballistic flow term over the grids. In order to avoid these oscillations, one should choose grid sizes Δx and Δt in such a way that they are always less than the characteristic scales in the problem, *i.e.*,

$$\Delta x \ll x_0 \quad \text{and} \quad \Delta t \ll t_0.$$

In view of the above, it is necessary to use the double Fourier transform to obtain an unambiguous picture of the structure factor and to pick out the asymptotic smoothing although this strategy might on first appearance seem to be a computational overkill. The overwhelming advantage is that, by scanning the structure factor as a function of frequency ω for a fixed k , one immediately sets two frequency scales ck and $D_h k^2$, thus making it possible to pick up the relevance of these scales in $S_h(k, \omega)$.

We also mention that our discussion is equally applicable to the Kardar-Parisi-Zhang (KPZ) equation [17] with the addition of a flow term. Here too, the use of the double Fourier transform reveals the presence of the ‘smoothing’ fixed point due to the flow term.

FIG. 1. The correlation function $S_h(k_i, \omega)$ against ω for three different wavevectors $k_1 = 0.02(\diamond)$, $k_2 = 0.08(+)$ and $k_3 = 0.12(\square)$ with parameters $c = 2.0$, $D_h = 1.0$ and $\Delta^2 = 1.0$. The positions of the peaks are given by $\omega_1 = 0.04$, $\omega_2 = 0.16$ and $\omega_3 = 0.24$ as expected from Eq.(5).

FIG. 2. The double Fourier transform, $S(k, \omega = 0)$ obtained from Eq.(4a) (Case A) for the h - h correlation function showing the crossover from high to low k . The different markers in the figure correspond to different grid sizes Δx to sample distinct regions of k space; thus the markers \triangle , \times , and \square correspond to decreasing grid sizes and increasing wavevector ranges. The parameters used in the calculation are $c = D_h = \Delta^2 = 1.0$ and the characteristic wavevector is $k_0 = \frac{c}{D_h} = 1.0$. The dashed line is a plot of $S_h(k, \omega = 0)$ vs k for Case A with appropriate parameters, to serve as a guide to the eye.

FIG. 3. The double Fourier transform, $S(k = 0, \omega)$ vs ω obtained from Eq.(4a) (Case A) for the h - h correlation function. The different markers in the figure correspond to different grid sizes Δt to sample distinct regions of ω space; thus the markers \triangle , \times , and \square correspond to decreasing grid sizes and increasing frequency ranges. The solid line is a plot of $S_h(k = 0, \omega)$ vs ω for Case A with appropriate parameters, to serve as a guide to the eye. The parameters are $c = D_h = \Delta^2 = 1.0$.

FIG. 4. Log-log plot of the single Fourier transform $S_h(k, t = 0)$ vs k obtained from Eq.(4a) (Case A) with parameters $c = D_h = \Delta^2 = 1.0$. The best fitted line shown in the figure is given by a slope of $-1 - 2\alpha_h = -1.90 \pm 0.016$. The characteristic wavevector k_0 is given by $k_0 = \frac{c}{D_h} = 1.0$

FIG. 5. (a) Log-log plot of the single Fourier transform $S_h(x = 0, \omega)$ vs ω obtained from Eq.(4a) showing a slow crossover. Lines 1 and 2 in the figure are the best fits in the low and high ω regions with slopes $-1 - 2\beta_h = -1.87 \pm 0.003$ and $-1 - 2\beta_h = -1.525 \pm 0.006$ respectively.

(b) Log-log plot of the single Fourier transform $S_h(x = 0, \omega)$ vs ω for two different values of c ; $c = 10$ and $c = 5$ for data sets 1 and 2 respectively. Note the increase in oscillation for increasing values of c . The other parameters are $D_h = \Delta^2 = 1.0$.

FIG. 6. (a) The behaviour of $\langle \rho(t) \rangle$ as a function of time t . Here $\langle \rho(t) \rangle$ is the average over the sandpile surface of 100 sample configurations. The grid size $\Delta t = 0.005$ and $c = \Delta^2 = D_h = 1.0$.

(b) The root mean square width $\rho_{rms}(t) = (\langle \rho^2 \rangle - \langle \rho \rangle^2)^{\frac{1}{2}}$ against time t over 100 sample configurations with parameters $c = \Delta^2 = D_\rho = D_h = 1.0$

(c) The variation of $\rho_{max}(t)$ and $\rho_{min}(t)$ with time t . $\rho_{max}(t)$ and $\rho_{min}(t)$ are respectively the maximum and minimum values of ρ for a given configuration of the sandpile at time t . Again, $c = D_h = D_\rho = \Delta^2 = 1.0$.

FIG. 7. One-loop diagrams for (a) $\Sigma_\rho(k, \omega)$, the self-energy in ρ , (b) $\Sigma_h(k, \omega)$, the self-energy in h for the coupled equations of Case B (Eq.(6)). (c) The glossary for the diagrams shown in Fig.7(a,b) and Fig.8. For example, the propagators for the h and ρ variables are represented by solid and dashed lines respectively, with a right arrow. Additionally there are diagrammatic definitions for the vertex and for the correlation functions for the h and ρ variables.

FIG. 8. One-loop diagrams for (a) $S_h(k, \omega)$, the $h - h$ correlation function, (b) $S_\rho(k, \omega)$, the $\rho - \rho$ correlation function for the coupled equations of Case B (Eq.(8)).

FIG. 9. Log-log plot of the single Fourier transform $S_h(k, t = 0)$ vs k obtained from Eqs.(6) (Case B). The best fit has a slope of $-1 - 2\alpha_h = -2.03 \pm 0.014$. Other parameters are $\mu = D_h = D_\rho = \Delta_h^2 = \Delta_\rho^2 = 1.0$.

FIG. 10. Log-log plot of the single Fourier transform $S_h(x = 0, \omega)$ vs ω for Case B obtained from Eqs.(6). The best fit shown in the figure has a slope of $-1 - 2\alpha_h = 1.93 \pm 0.017$. Again $\mu = D_h = D_\rho = \Delta_h^2 = \Delta_\rho^2 = 1.0$.

FIG. 11. The double Fourier transform $S_h(k_i, \omega)$ vs ω (Case B) calculated at two different wavevectors $k_i = 0.1(\diamond), 0.2(+)$. The curves (solid(1) and dashed(2) lines) shown in the figure are plots of Eq.(18) with $\Gamma_0 = 0.4$ and 0.5 (for k_1 and k_2 respectively), to serve as a guide to the eye. Other parameters are $\mu = 2, \Delta_h^2 = \Delta_\rho^2 = 0.1, D_h = D_\rho = 1.0$.

FIG. 12. Log-log plot of the double Fourier transform $S_h(k, \omega = 0)$ vs k (Case B) obtained from Eqs.(6). The best fit has a slope of $-(1 + 2\alpha_h + z_h) = -3.40 \pm 0.029$. Again, $\mu = 1.0, D_h = D_\rho = 1.0, \Delta_h^2 = \Delta_\rho^2 = 0.5$.

FIG. 13. Log-log plot of the double Fourier transform $S_h(k = 0, \omega)$ vs ω obtained from Eqs.(6) (Case B). The best fit displayed in the figure has a slope of $-(1 + 2\beta_h + \frac{1}{z_h}) = -1.91 \pm 0.017$. Other parameters are $\mu = 1.0, D_h = D_\rho = 1.0, \Delta_h^2 = \Delta_\rho^2 = 0.5$.

FIG. 14. Log-log plot of the single Fourier transform $S_\rho(x = 0, \omega)$ vs ω obtained from Eqs.(6) (Case B). The best fit has a slope of $-1 - 2\beta_\rho = -1.81 \pm 0.017$. Again, $\mu = 1.0, D_h = D_\rho = 1.0, \Delta_h^2 = \Delta_\rho^2 = 0.5$.

FIG. 15. Log-log plot of the single Fourier transform $S_\rho(k, t = 0)$ vs k (Case B) showing a crossover from a slope of $-1 - 2\alpha_\rho = 0$ at small k to -2.12 ± 0.017 at large k . Other parameters are $\mu = 1.0, D_h = D_\rho = 1.0, \Delta_h^2 = \Delta_\rho^2 = 0.5$.

FIG. 16. One-loop corrections to (a) the KPZ vertex, and (b) the λ vertex for the coupled equations of Case C (Eqs.(21)).

FIG. 17. Log-log plot of the single Fourier transform $S_h(k, t = 0)$ vs k for Case C obtained from Eqs.(21). The slope of the fitted line is given by $-1 - 2\alpha_h = -2.56 \pm 0.060$. The parameters used in the simulation are $\nu = 10, \lambda = 1.0, D_h = D_\rho = 1.0, \Delta_h^2 = 1.0$.

FIG. 18. Log-log plot of the single Fourier transform $S_h(x = 0, \omega)$ vs ω obtained from Eqs.(21) (Case C). The best fit has a slope of $-1 - 2\beta_h = -1.68 \pm 0.011$ with parameters $\nu = 10, \lambda = 1.0, D_h = D_\rho = 1.0, \Delta_h^2 = 1.0$.

FIG. 19. Log-log plot of the double Fourier transform $S_h(k, \omega = 0)$ vs k obtained from Eqs.(21) (Case C). The best fit for high wavevector has a slope of $-(1 + 2\alpha_h + z_h) = -4.54 \pm 0.081$. As $k \rightarrow 0$ we observe a crossover to slope of zero. Other parameters are $D_h = D_\rho = 1.0, \Delta_h^2 = 1.0, \nu = 10$ and $\lambda = 1.0$.

FIG. 20. Log-log plot of the double Fourier transform $S_h(k=0, \omega)$ vs ω obtained from Eqs.(21) (Case C). The best fitted line shown in the figure has a slope of $-(1 + 2\beta_h + \frac{1}{z_h}) = -1.80 \pm 0.007$. Other parameters are $D_h = D_\rho = 1.0, \Delta_h^2 = 1.0, \nu = 10$ and $\lambda = 1.0$.

FIG. 21. The double Fourier transform $S_h(k_i, \omega)$ vs ω obtained from Eqs.(21) (Case C) evaluated at three different wavevectors $k_1 = 0.2(\diamond)$, $k_2 = 0.4(+)$ and $k_3 = 0.8(\square)$ with parameters $D_h = D_\rho = 1.0, \Delta_h^2 = 1.0, \nu = 5$ and $\lambda = 1.0$. The peaks correspond to frequencies $\omega_1 = 1.0, \omega_2 = 2.0, \omega = 4.0$.

FIG. 22. Log-log plot of the single Fourier transform $S_h(k, t=0)$ vs k obtained from the mean-field Eqs.(24a,24b). The high k region is fitted with a line of slope $-1 - 2\alpha_h = -2.05 \pm 0.017$. The low k region is fitted with a line of slope $-1 - 2\alpha_h = -0.93 \pm 0.024$. Note the crossover from $\alpha_h = 0.5$ at large k to zero at small k . Other parameters are $\nu' = 10, \lambda' = 2.0, D_h = D_\rho = 1.0, \Delta_h^2 = 0.1$.

FIG. 23. Log-log plot of the single Fourier transform $S_h(x=0, \omega)$ vs ω for the mean-field Eqs.(24a,24b). The best fit has a slope of $-1 - 2\beta_h = -1.94 \pm 0.001$ with parameters $\nu' = 10, \lambda' = 2.0, D_h = D_\rho = 1.0, \Delta_h^2 = 0.1$.

Fig.1

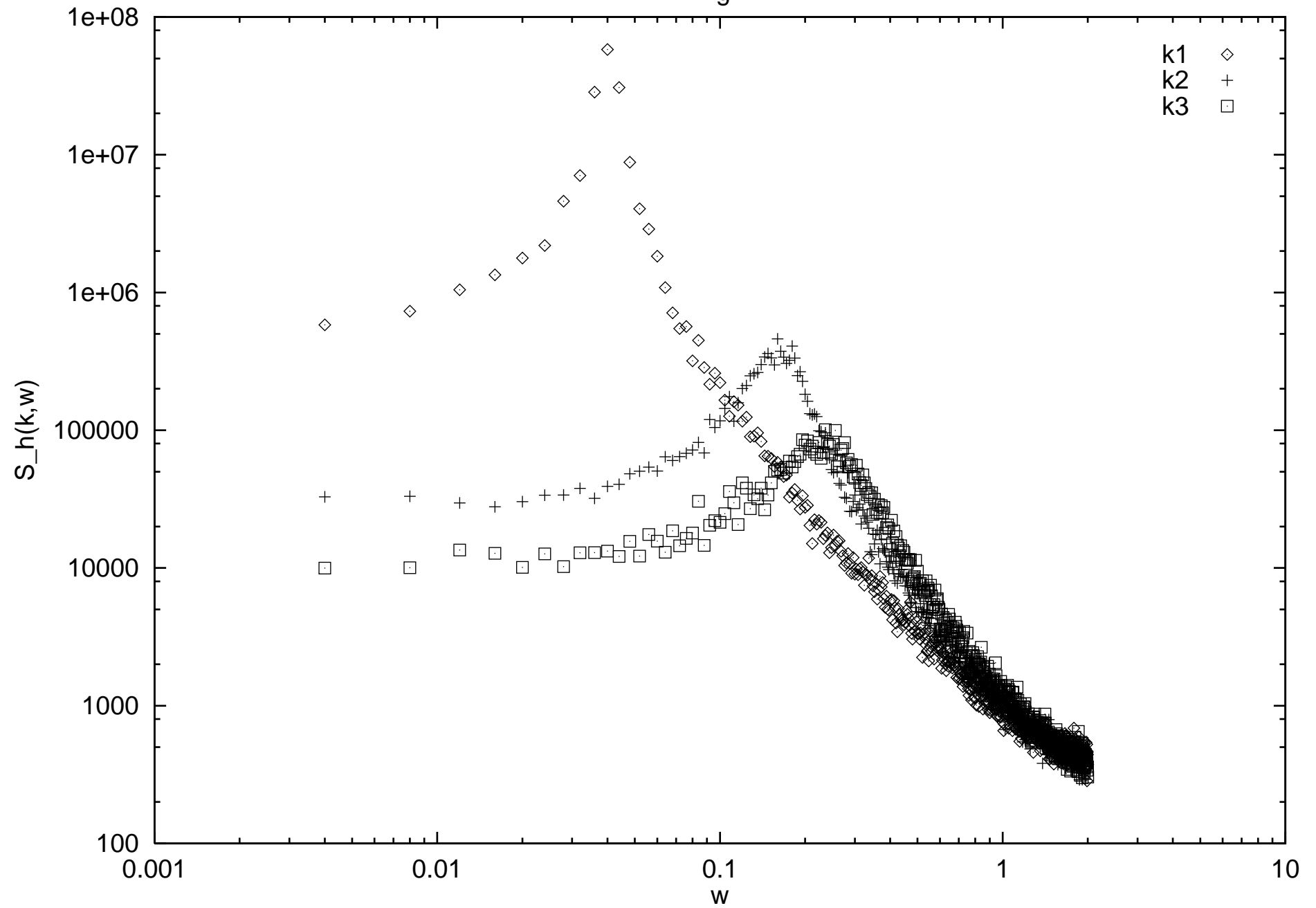


Fig.2

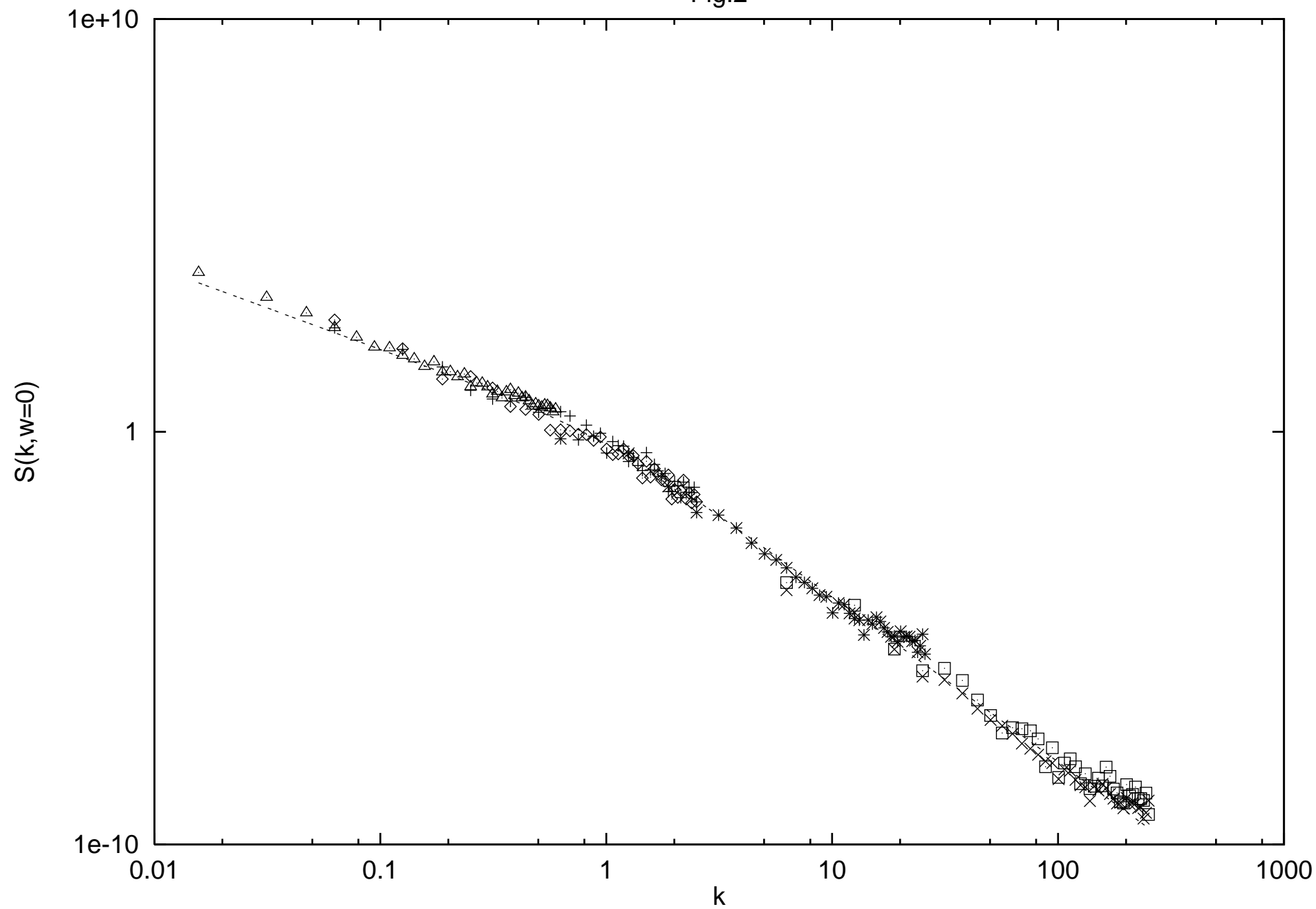


Fig.3

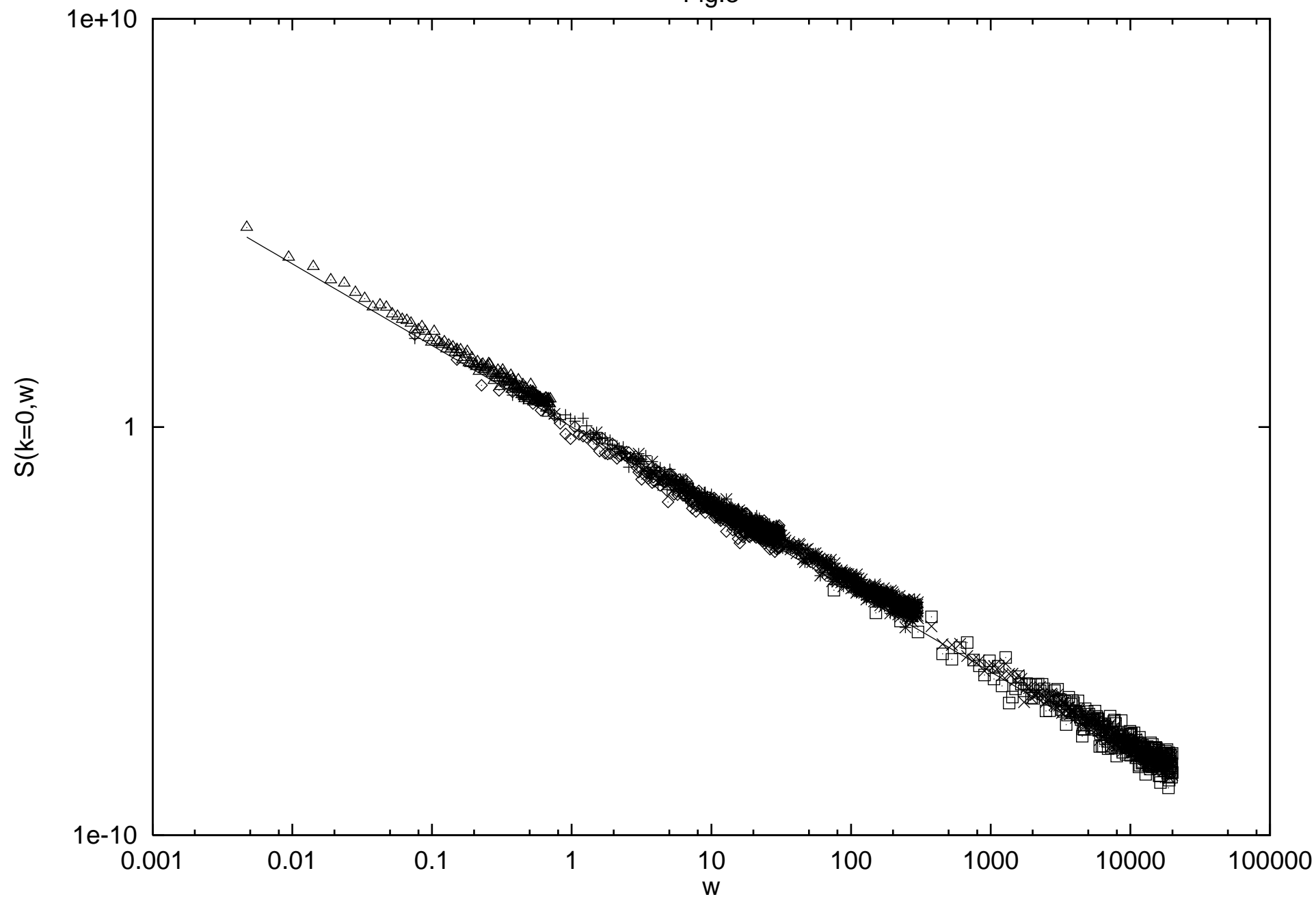


Fig.4

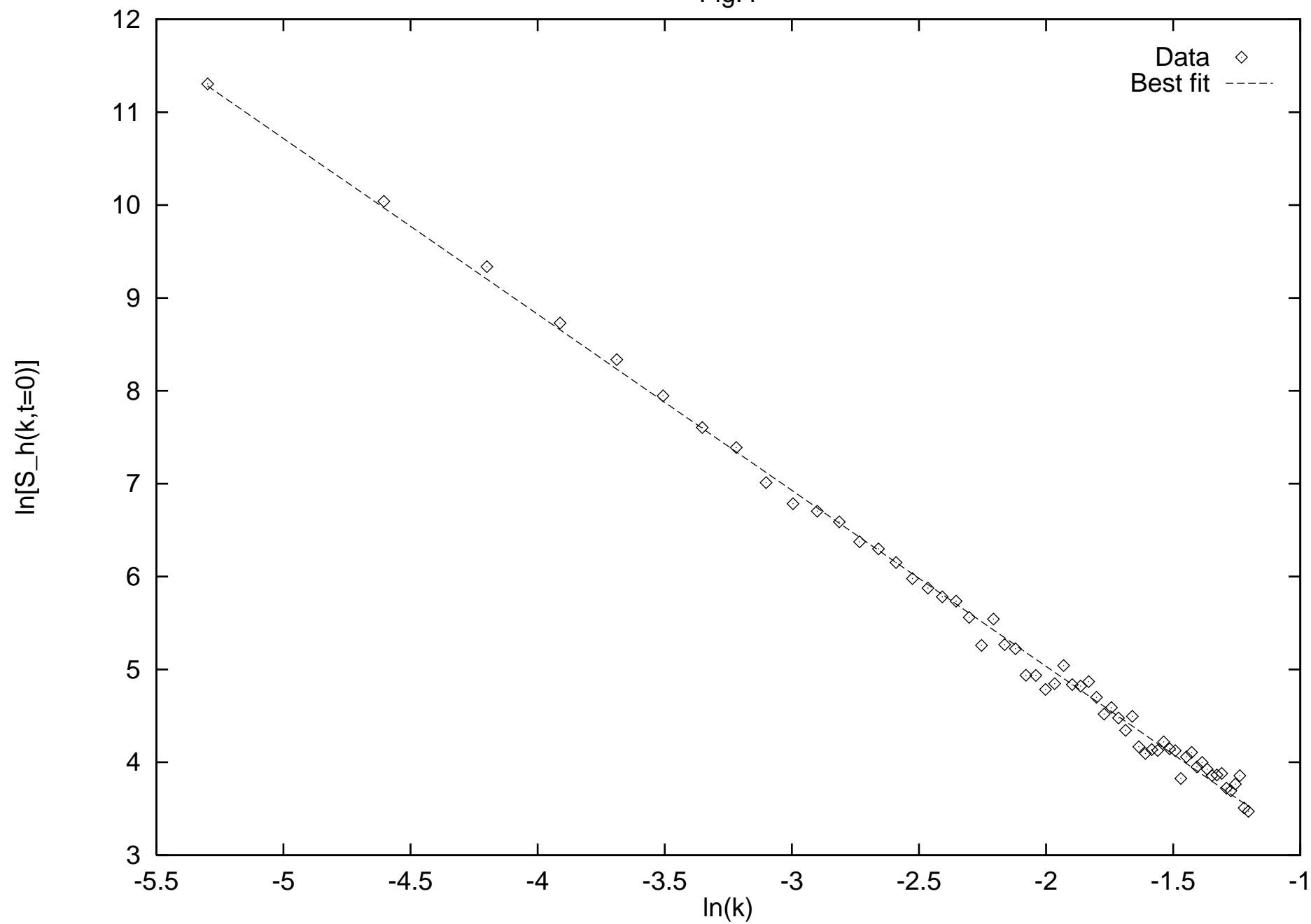


Fig.5(a)

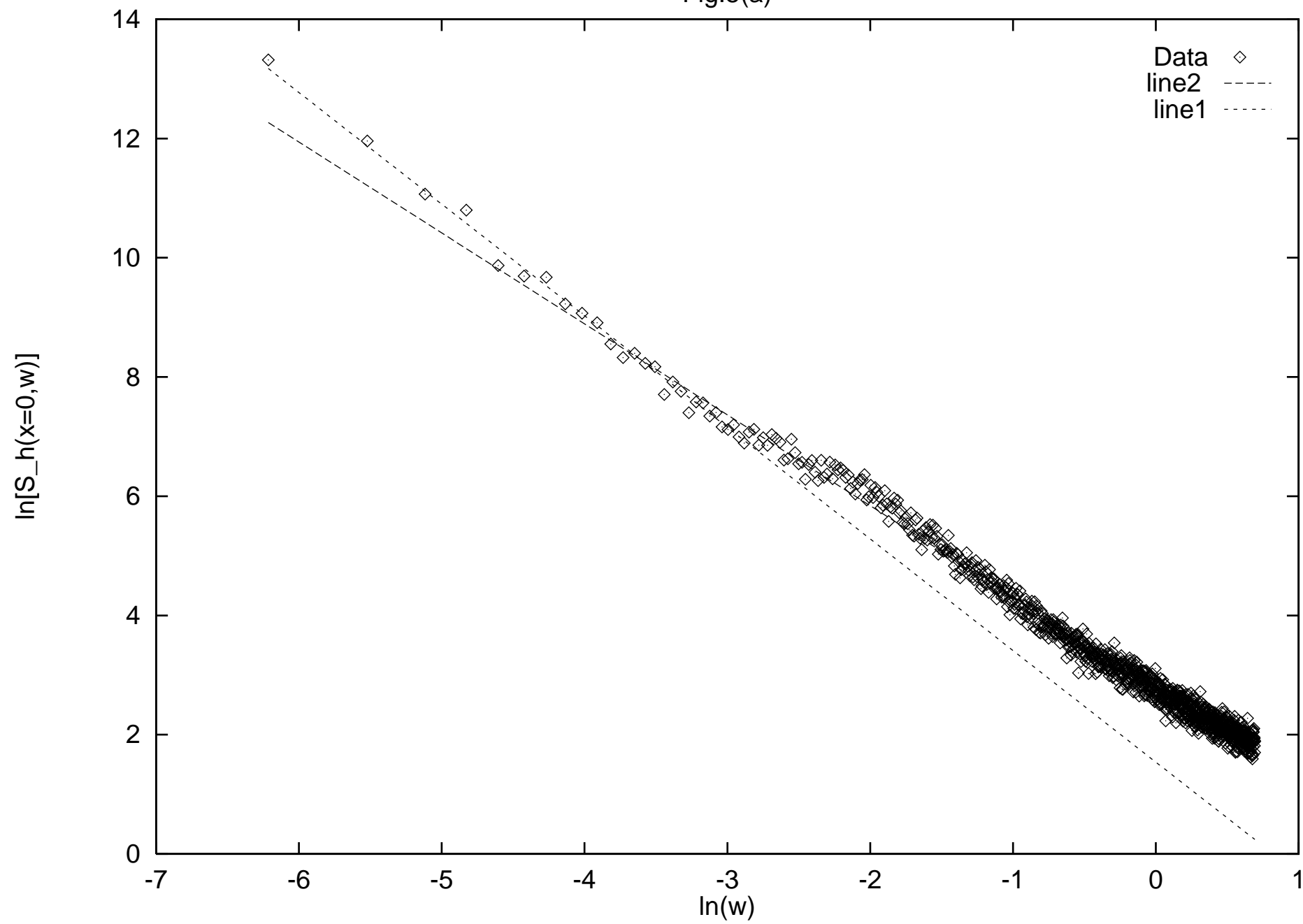


Fig.5(b)

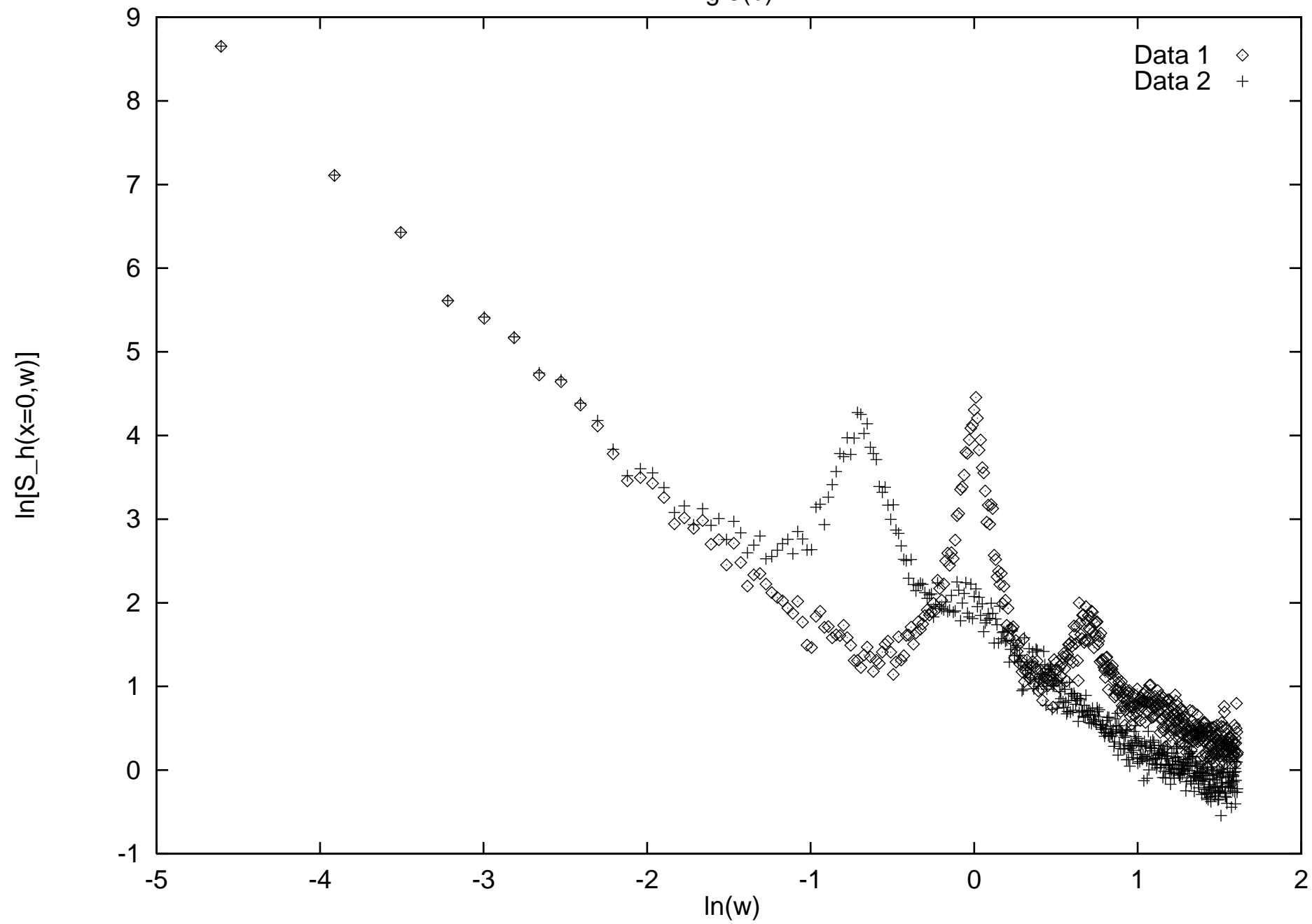


Fig.6(a)

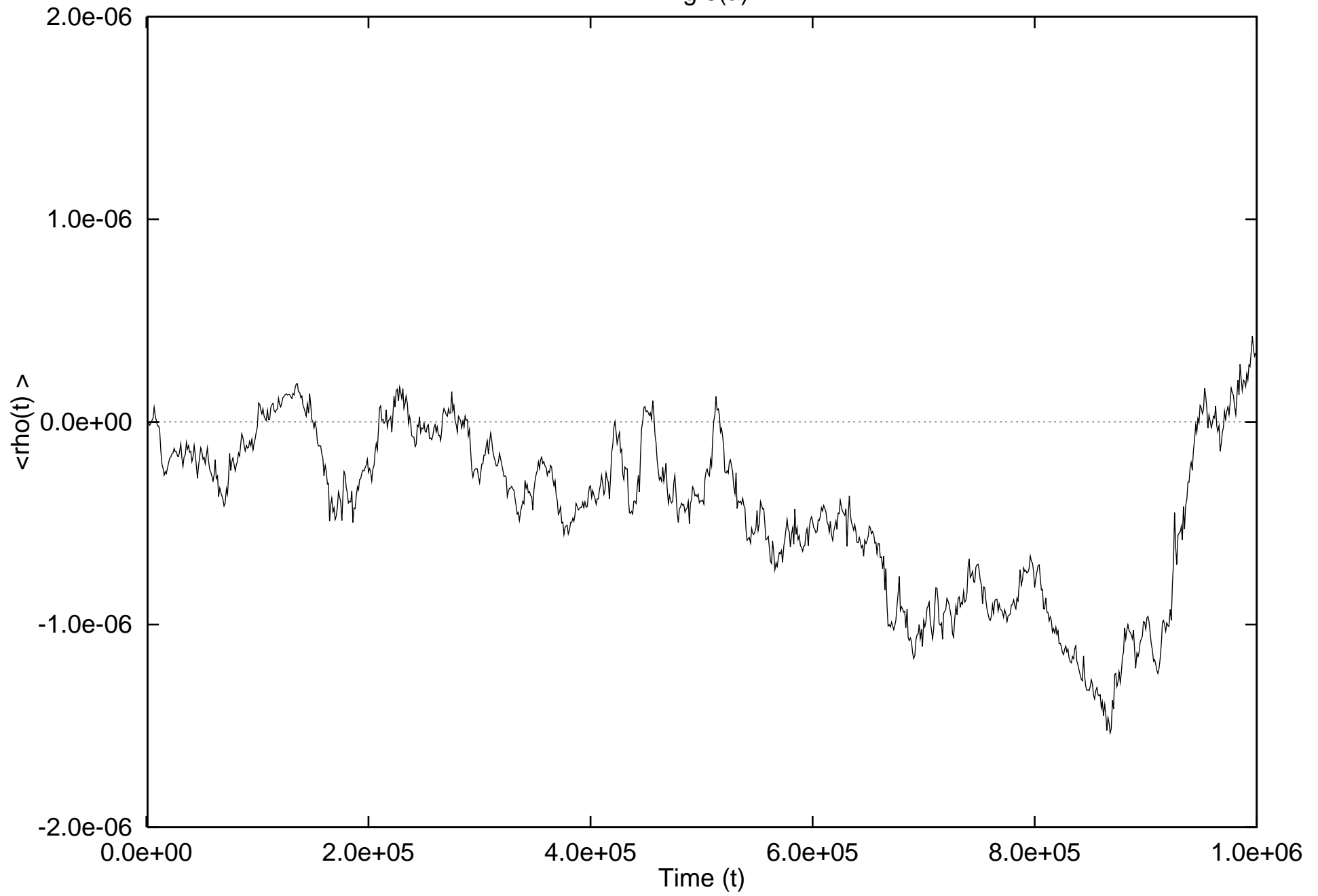


Fig.6(b)

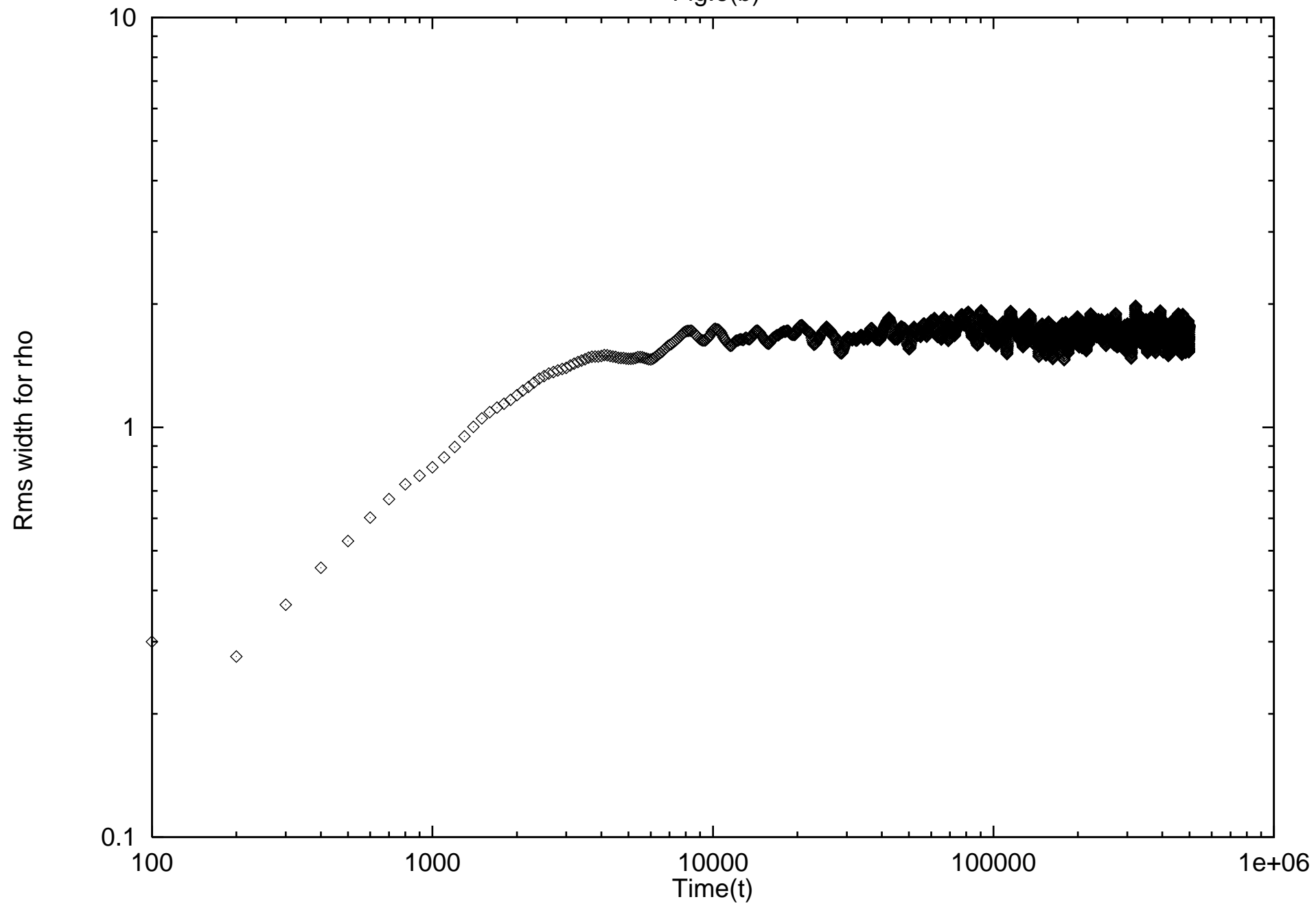
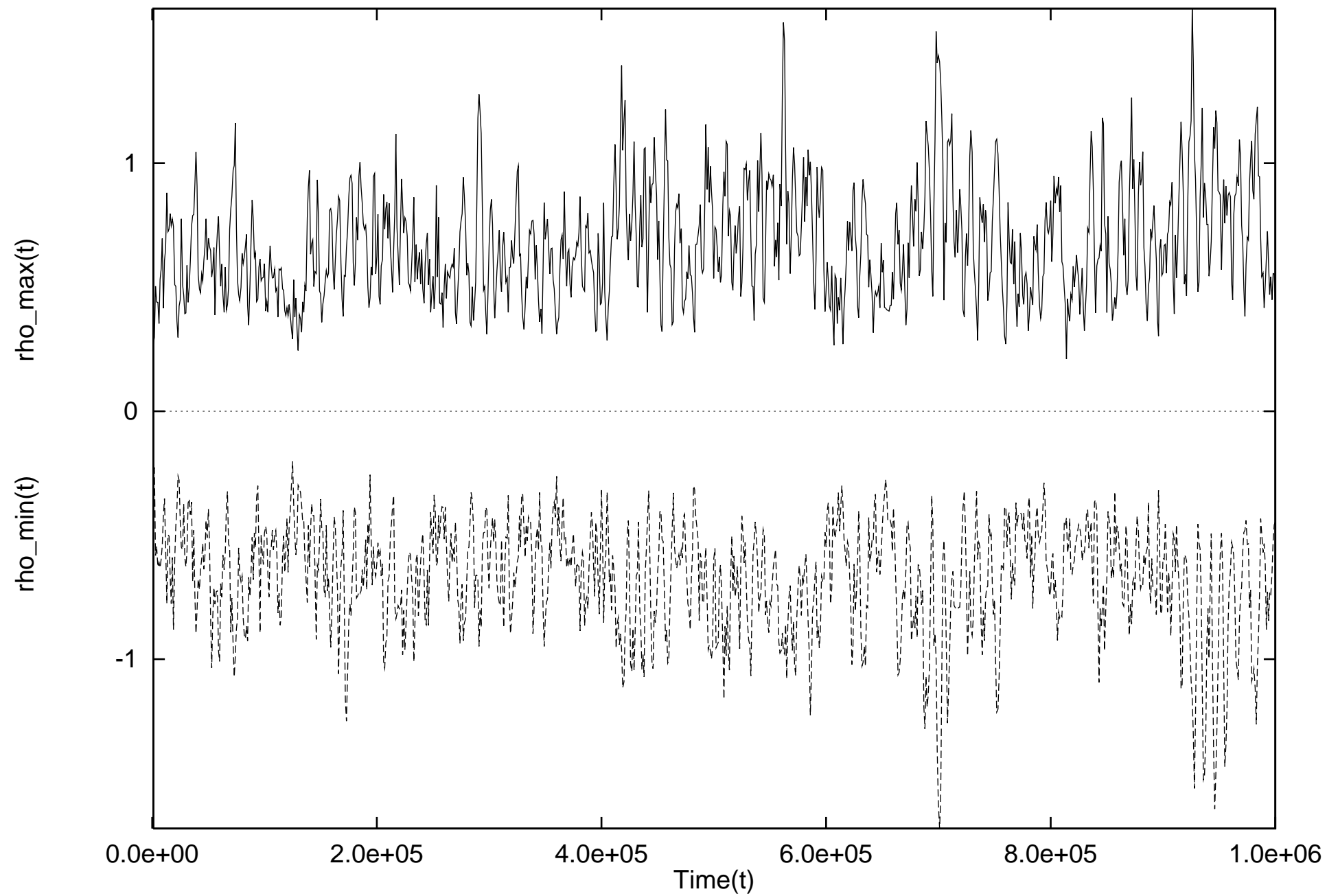


Fig.6(c)



$$\Sigma_{\rho}(k, \omega) =$$

(a)

$$\Sigma_h(k, \omega) =$$

(b)

$$\begin{array}{c} k \quad \omega \\ \hline \end{array}$$

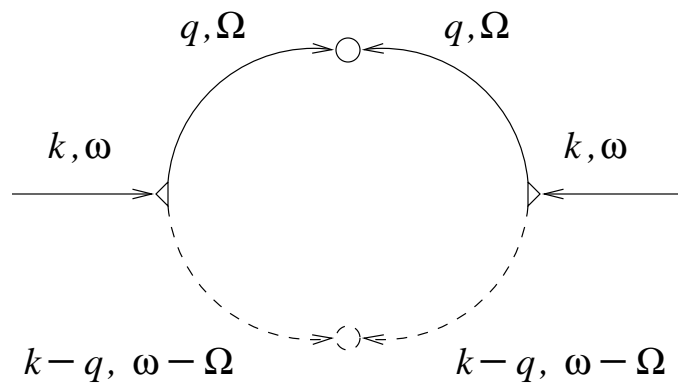
$$\frac{k}{\omega} \geq \frac{k}{\omega}$$

$$\xrightarrow{k} \omega$$

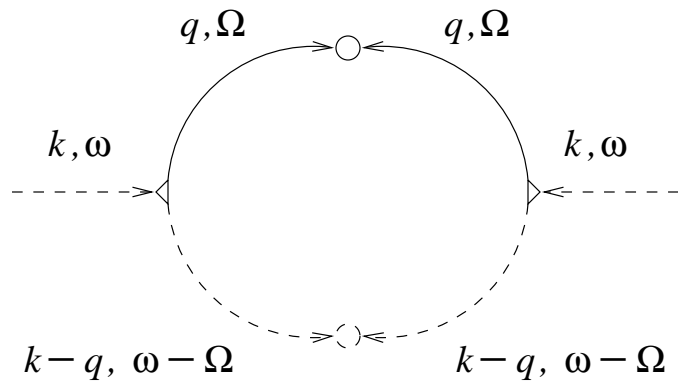
A diagram showing a vertex where an incoming line with momentum k and energy ω splits into two outgoing lines with momenta $k-q$ and $\omega-\Omega$.

(c)

Fig. 7



(a)



(b)

Fig. 8

Fig.9

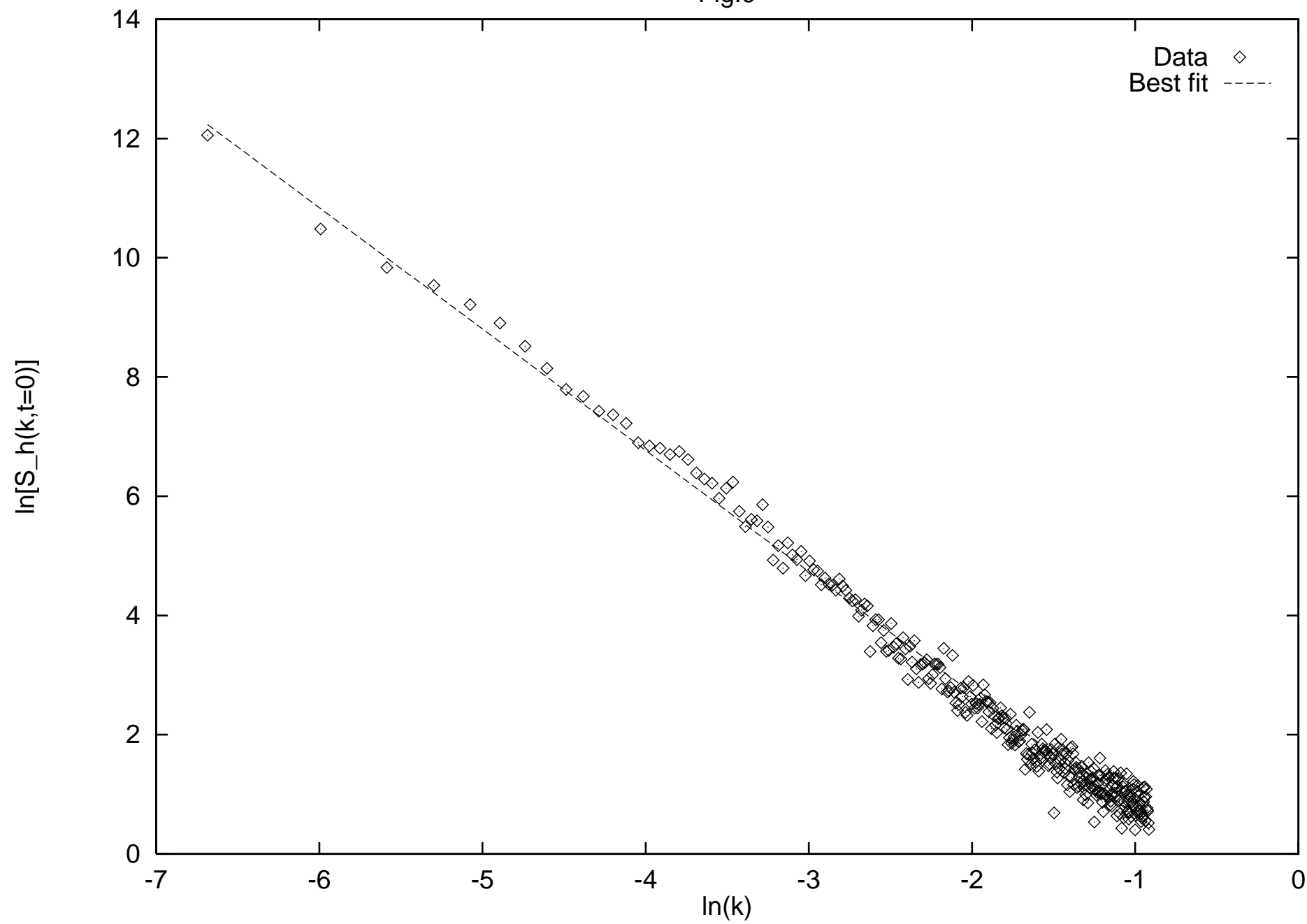


Fig.10

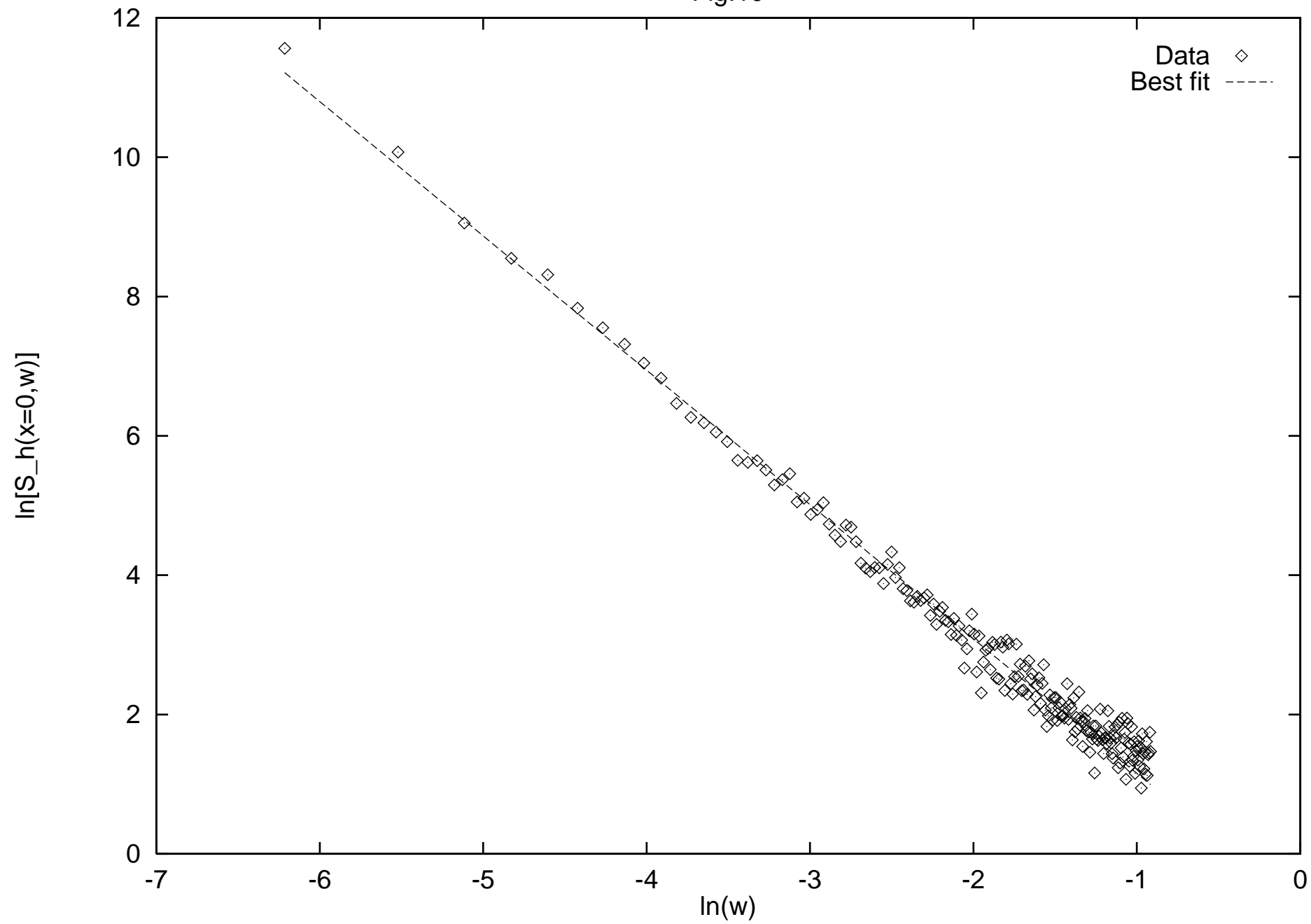


Fig.11

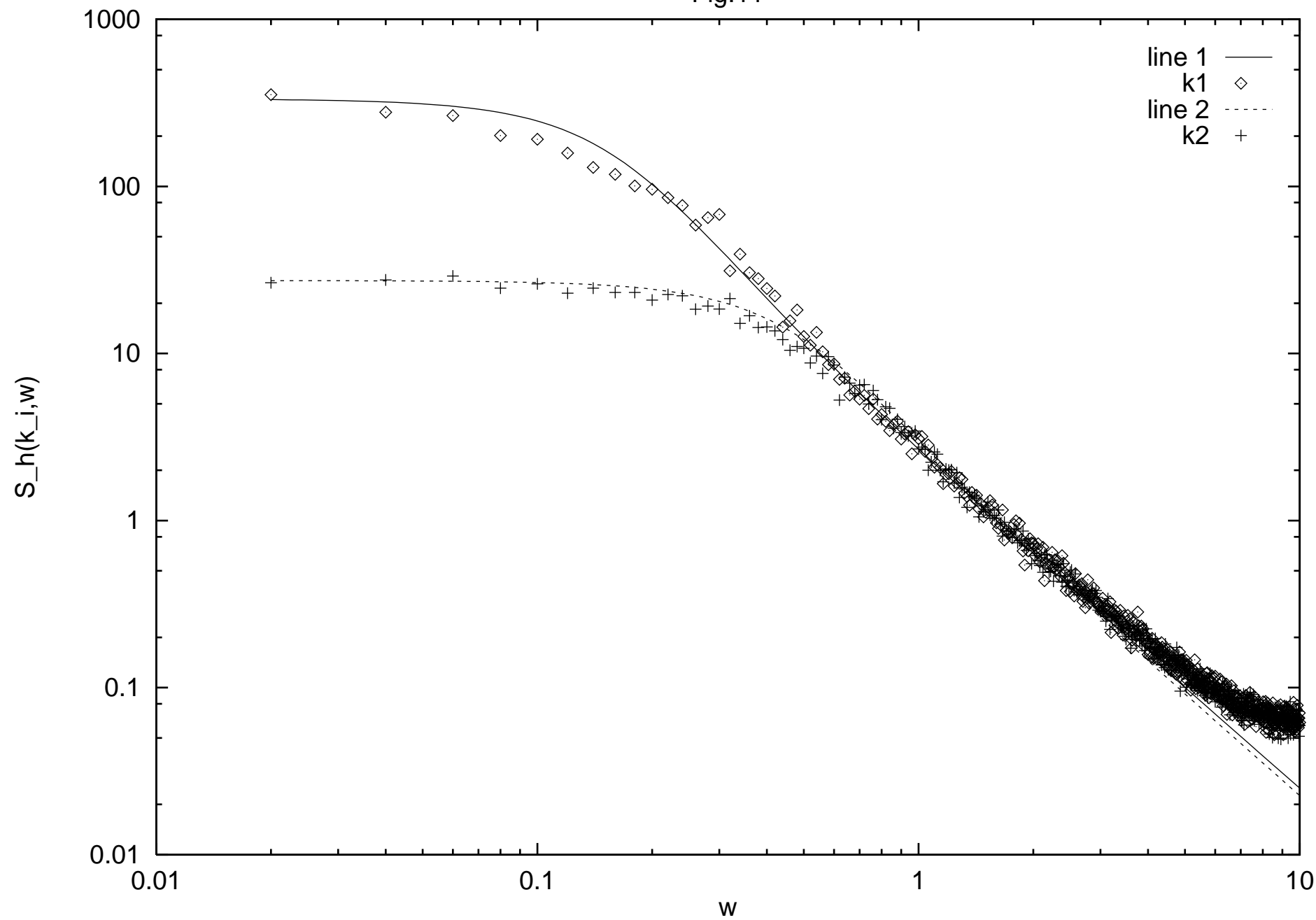


Fig.12

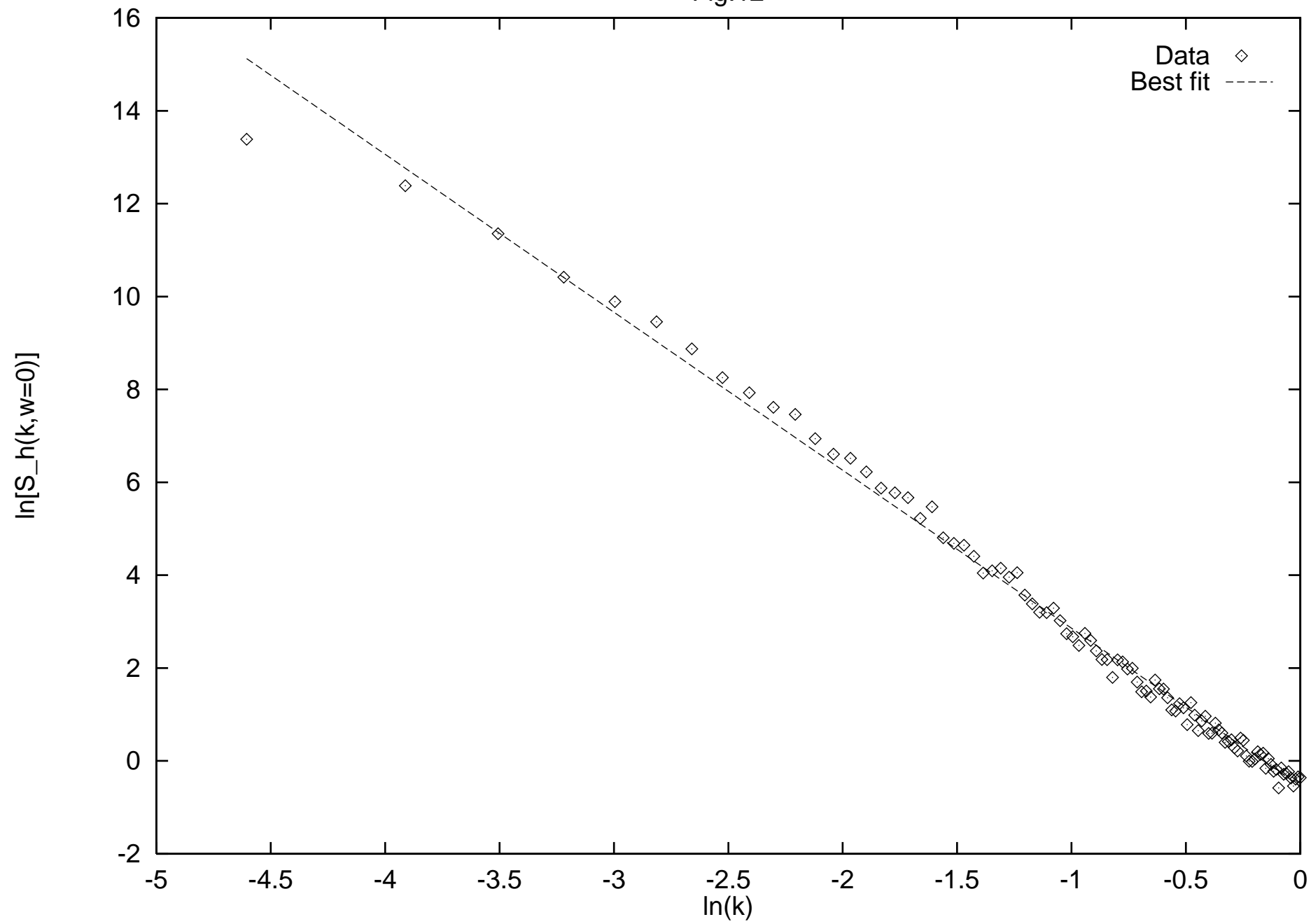


Fig.13

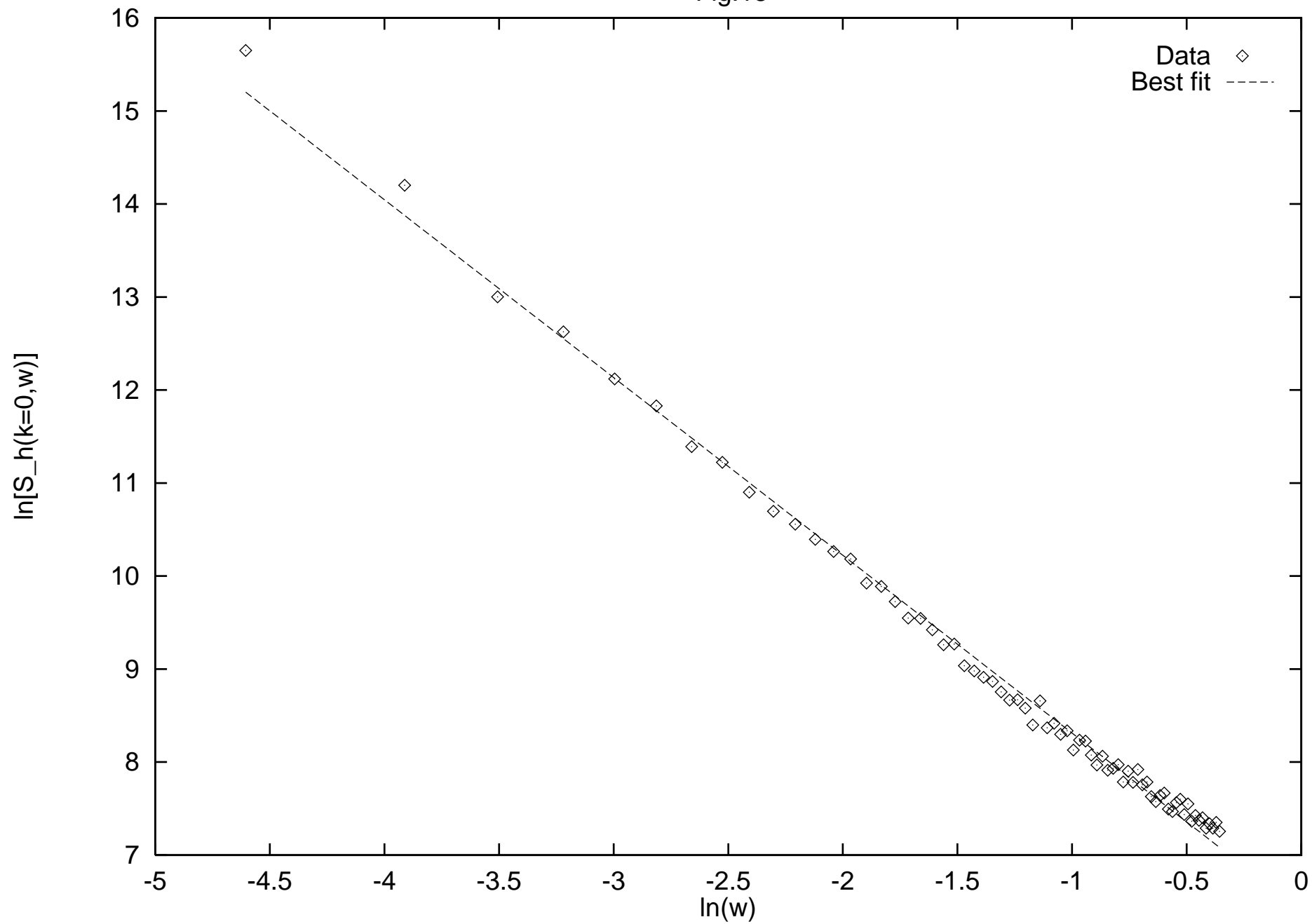


Fig.14

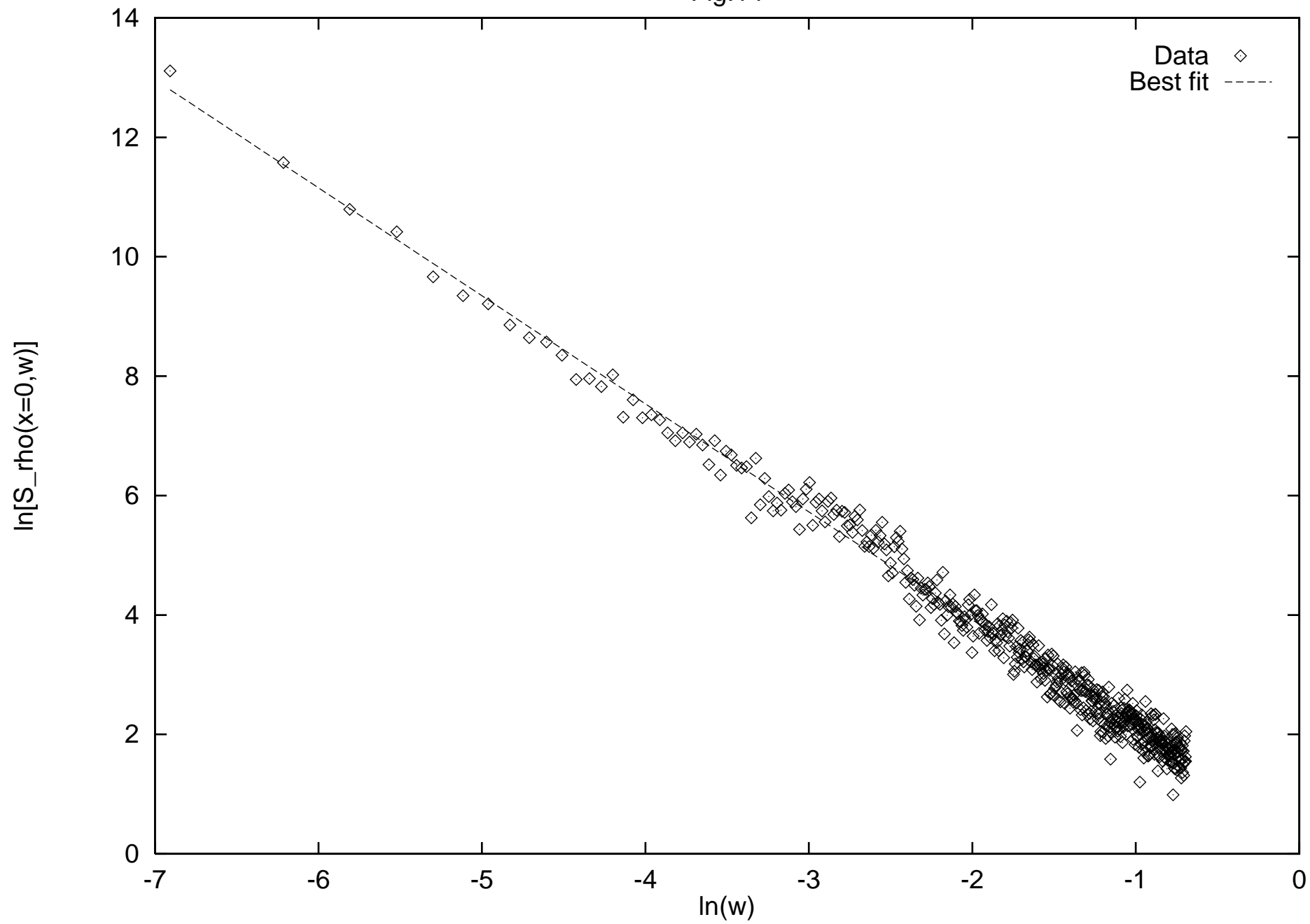
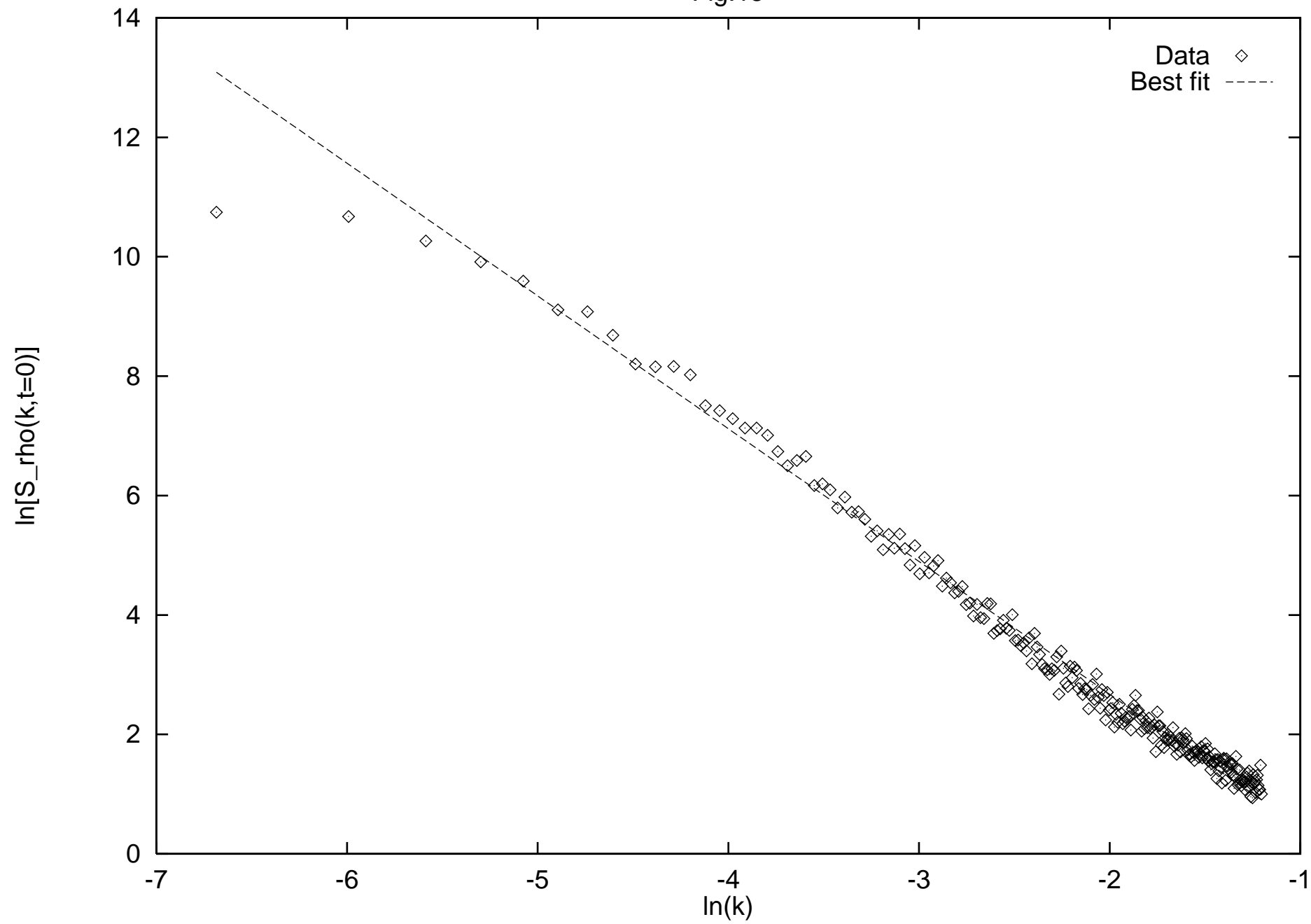
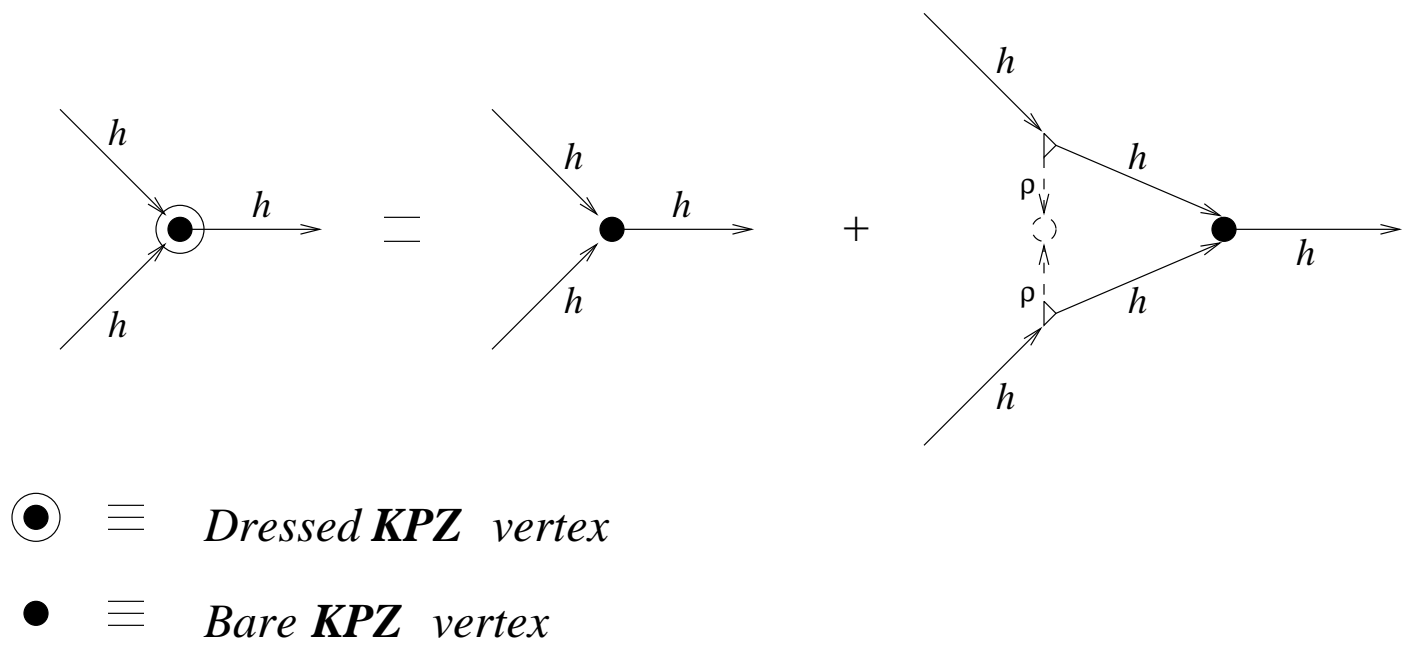
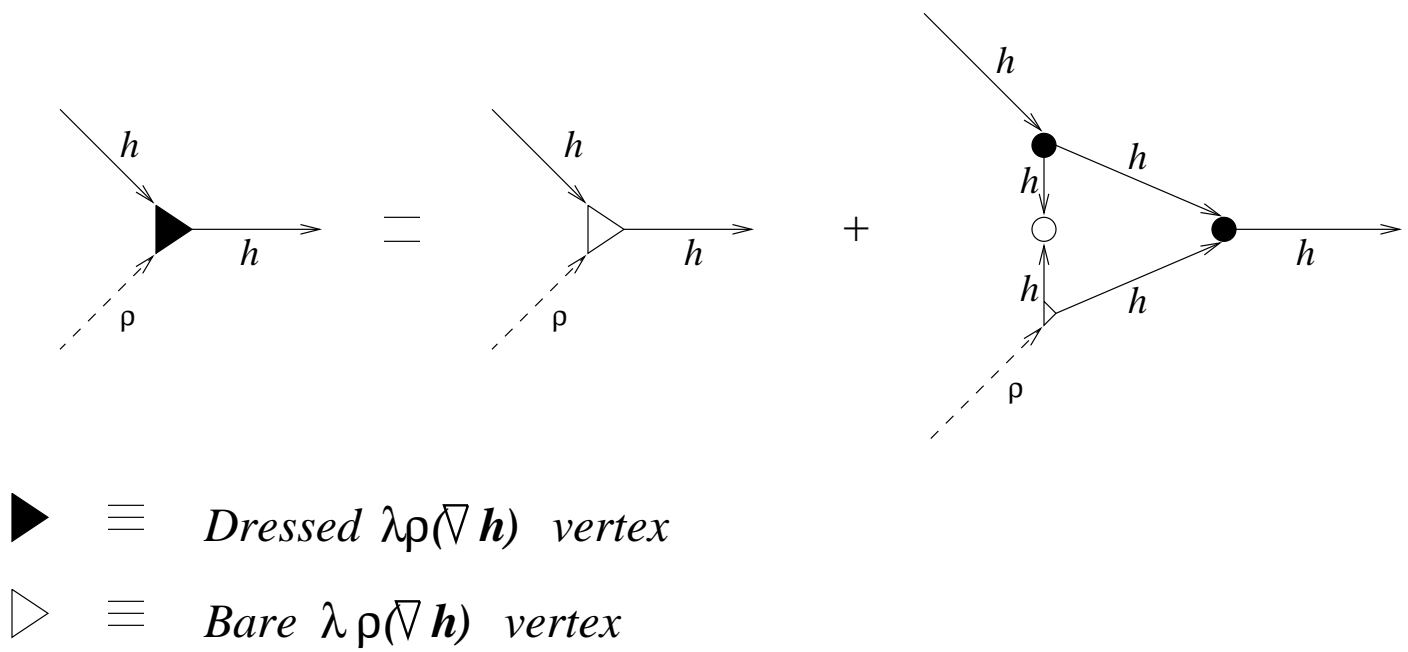


Fig.15





(a)



(b)

Fig. 16

Fig.17

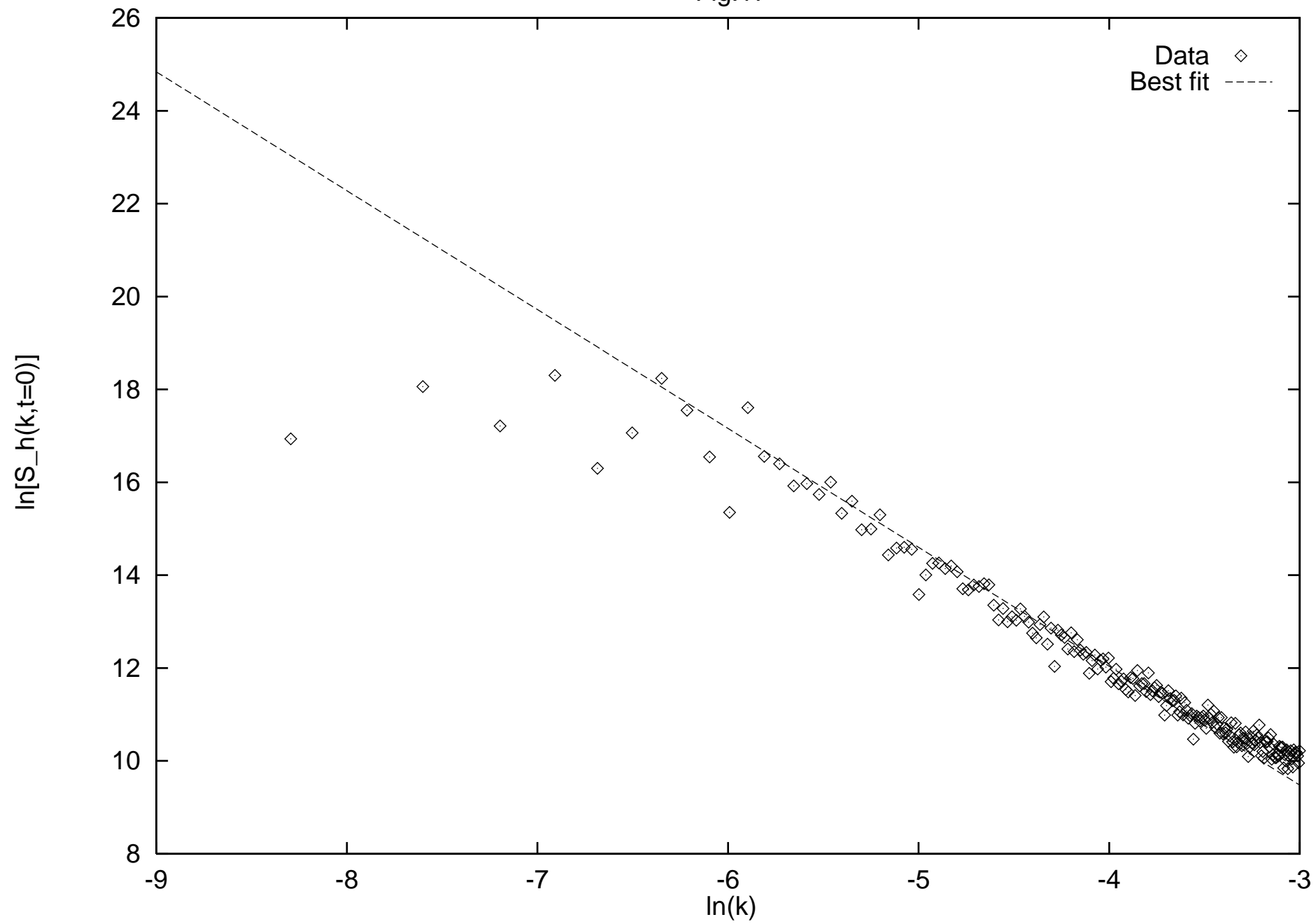


Fig.18

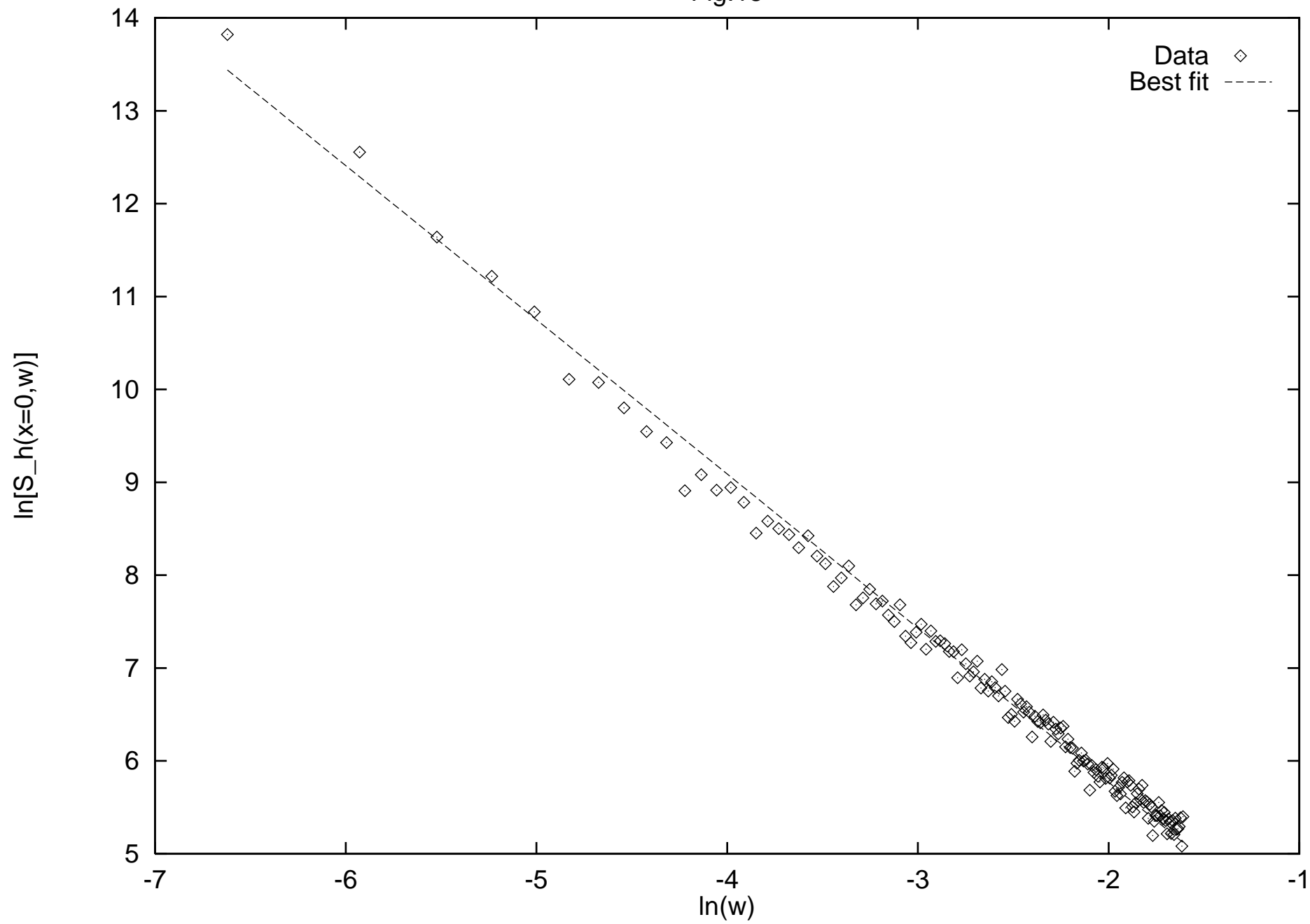


Fig.19

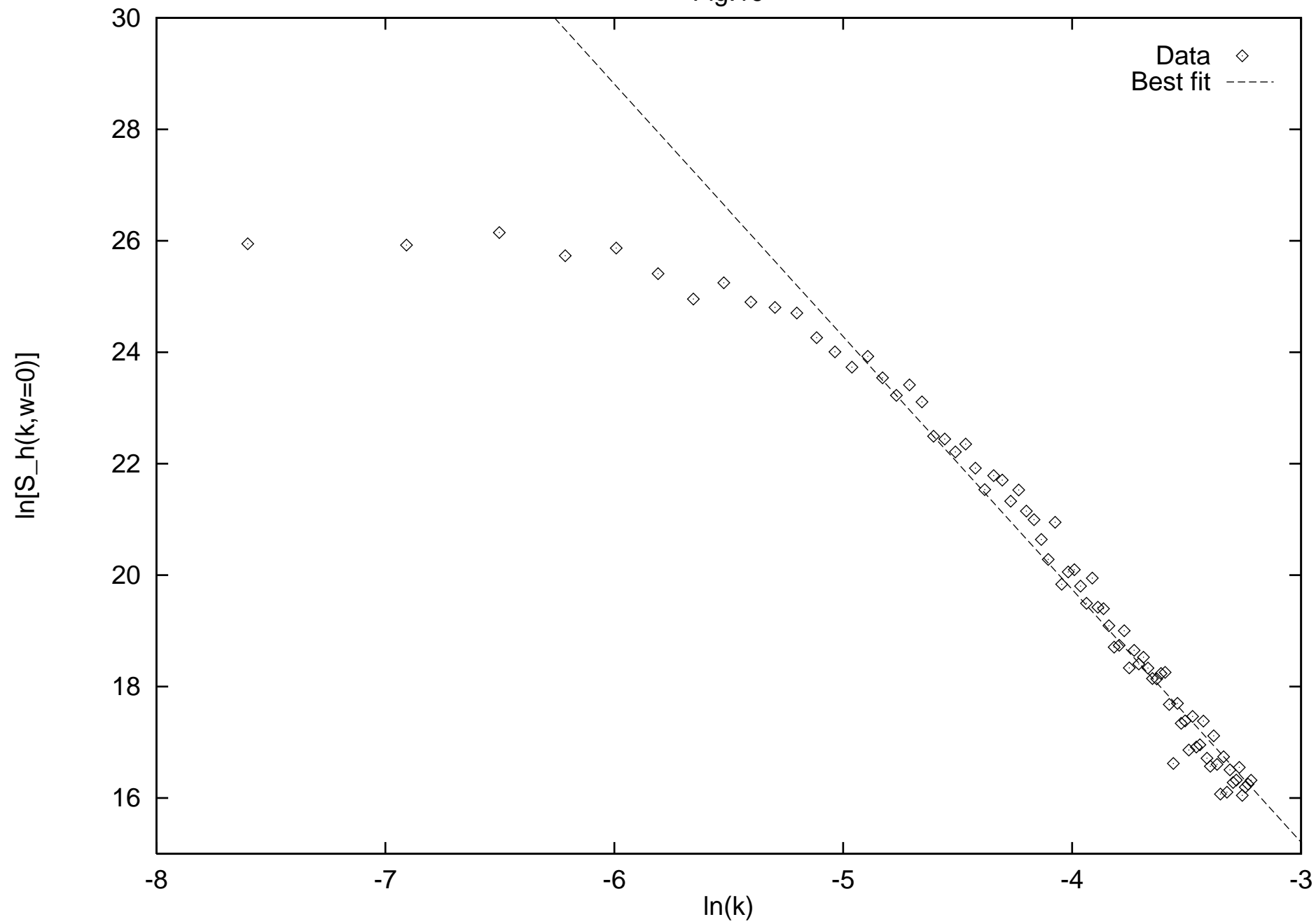


Fig.20

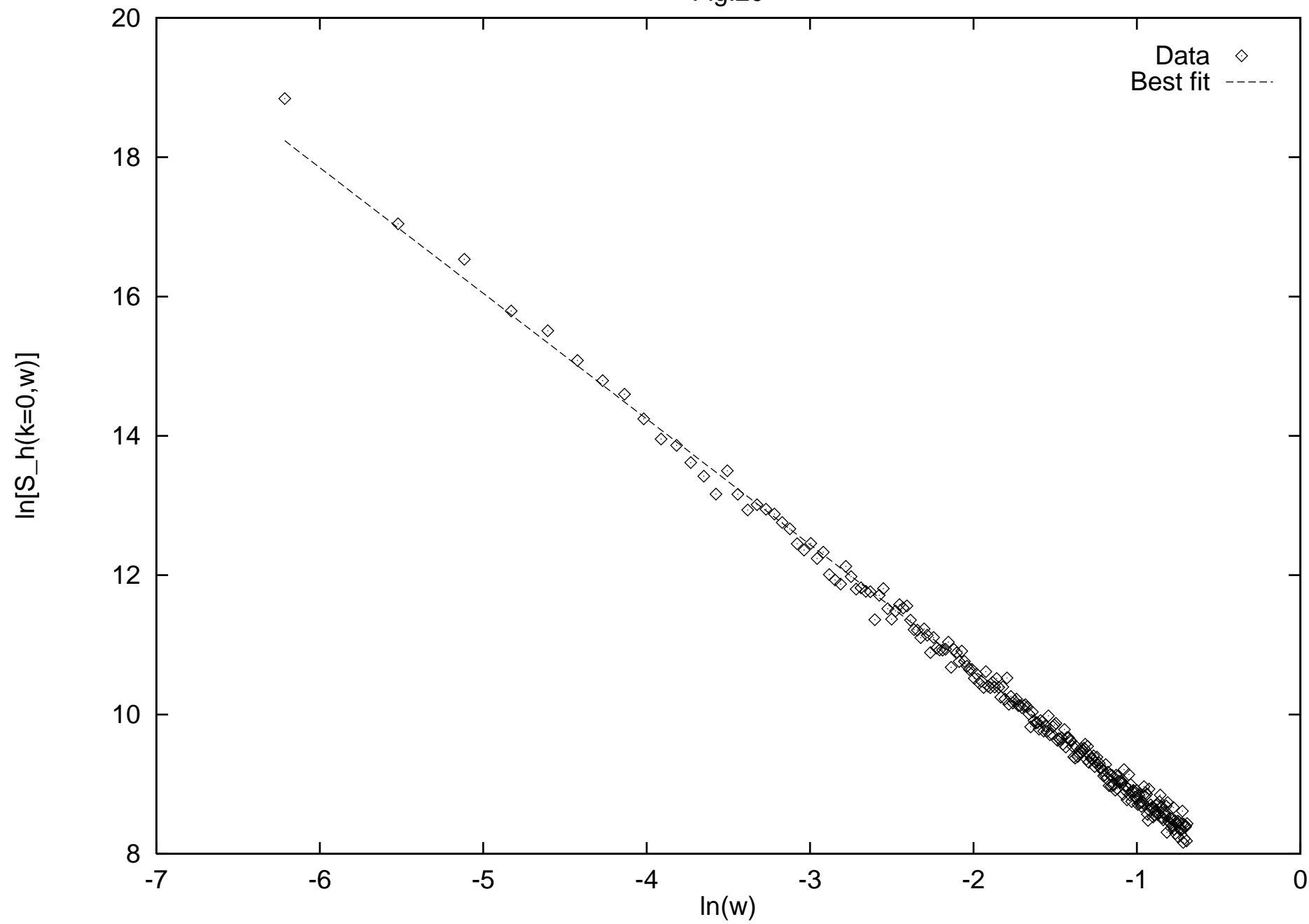


Fig.21

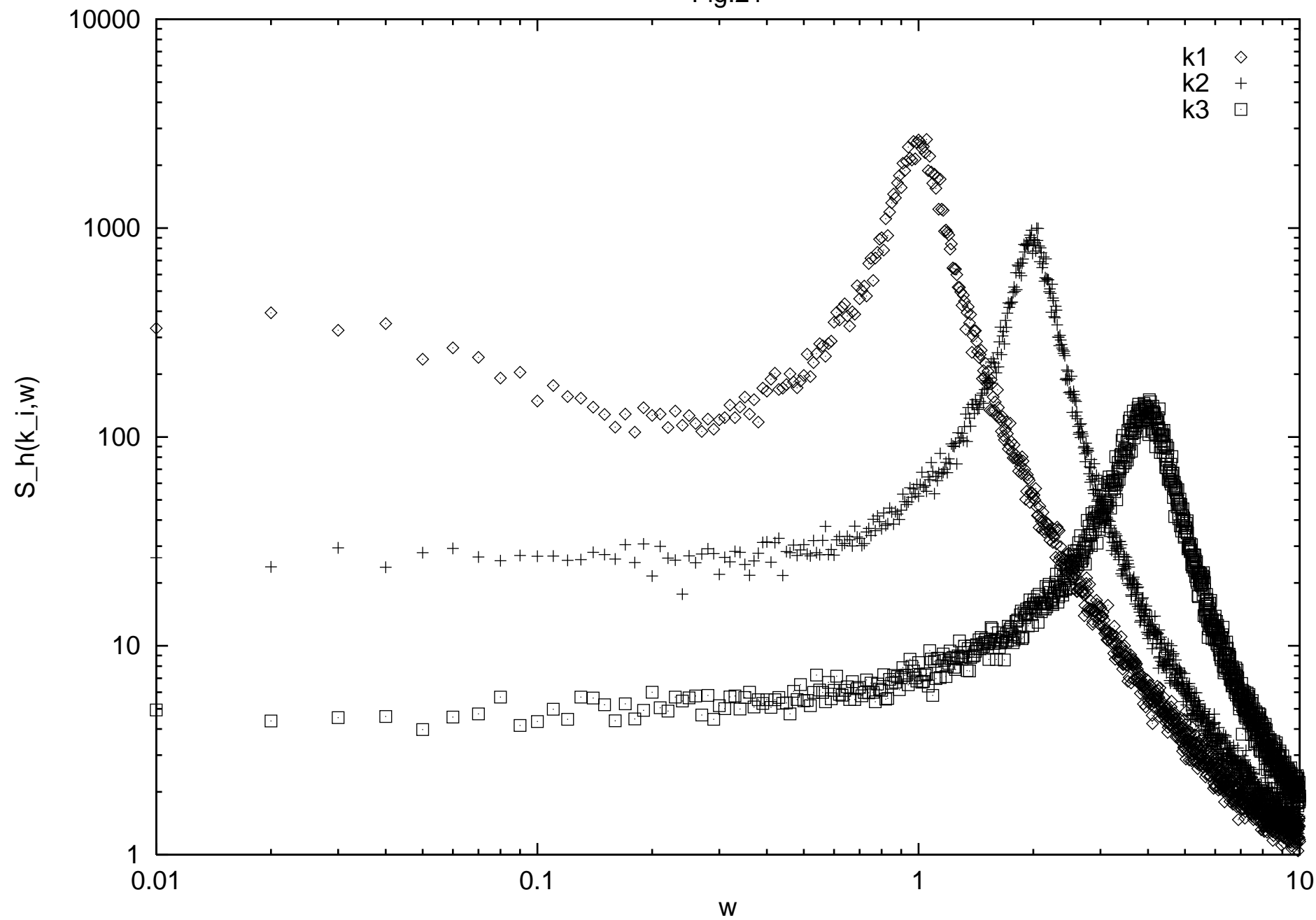


Fig.22

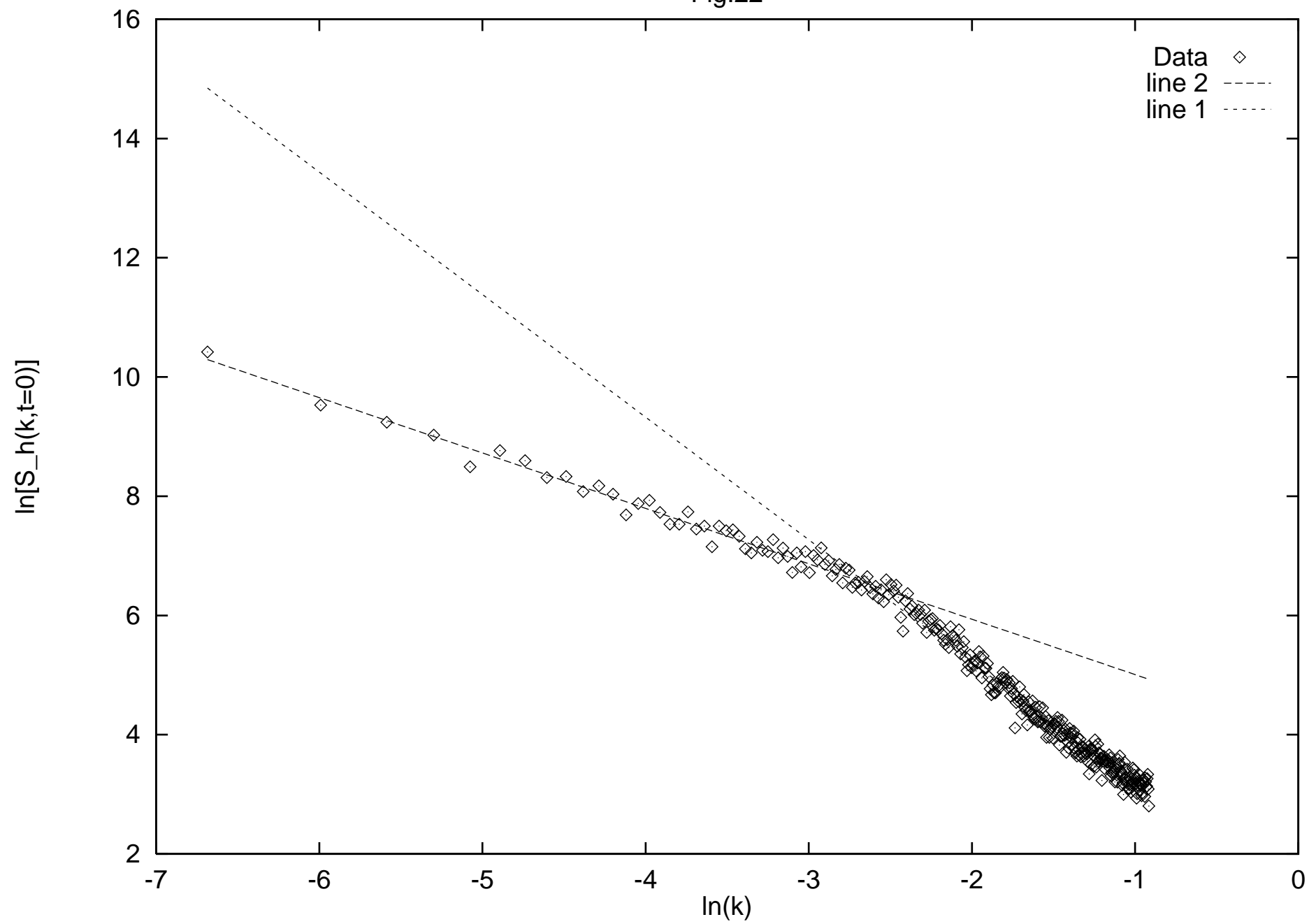


Fig.23

